Predicting the Time-of-Arrival of Coronal Mass Ejections at Earth Solely From Heliospheric Imaging Observations

Carlos Roberto Braga[1], Angelos Vourlidas[2], Guillermo Stenborg[3], Alisson Dal Lago[4], Rafael R. S. Mendonca[5], and Ezequiel Echer[4]

[1]George Mason University
[2]JHU APL
[3]Unknown
[4]National Institute for Space Research (INPE)
[5]INPE - National Institute for Space Research

November 21, 2022

Abstract

The Time-of-Arrival (ToA) of coronal mass ejections (CME) at Earth is a key parameter due to the space weather phenomena associated with the CME arrival, such as intense geomagnetic storms. Several approaches to estimate the ToA based on kinematical parameters derived from single- and multi-viewpoint white-light coronagraph observations have been proposed and implemented, particularly in the last decade. Despite the incremental use of new instrumentation and the development of novel methodologies, ToA estimated errors remain above 10 hours on average. Here, we investigate the prediction of ToA of CMEs using observations solely from heliospheric imagers, i.e., from heliocentric distances higher than those covered by the existent coronagraphs. To that aim, we analyse 14 CMEs observed by the heliospheric imager HI-1 onboard the twin STEREO spacecraft to determine their front location and speed. Outside the field of view of the instruments, we assume that the dynamics of the CME evolution is controlled by the aerodynamic drag, a force that comes from the interaction with particles from the background solar wind. We found a CME ToA error mean value of 0.4+-7.3 hours ToA and a mean absolute error of 6.1+-3.6 hours in a set of 14 events. The results we found here illustrate that observations from HI-1 allow us to estimate the ToA with similar errors than observations from coronagraphs.

Predicting the Time-of-Arrival of Coronal Mass Ejections at Earth Solely From Heliospheric Imaging Observations

Carlos Roberto Braga [1,2], Angelos Vourlidas [2], Guillermo Stenborg [3], Alisson Dal Lago [4], Rafael Rodrigues Souza de Mendonça [4], Ezequiel Echer [4]

[1]George Mason University, 4400 University Drive, Fairfax, VA, 22030, USA

[2]The Johns Hopkins University Applied Physics Laboratory, Laurel, MD 20723, USA

[3]Space Science Division, U.S. Naval Research Laboratory, 4555 Overlook Ave. SW Washington, DC 20375, USA

[4]National Institute for Space Research, Av. dos Astronautas, 1758, São José dos Campos, 12227-010, SP, Brazil

Key Points:

- We studied CME propagation relying only observations from the Heliospheric Imager 1
- We derived a CME Time-of-Arrival mean absolute error of 6.1 hours for a set of 14 events
- The CME Time-of-arrival error derived here is comparable to results from coronagraphs

Corresponding author: Carlos Roberto Braga, cbraga@gmu.edu

Abstract

The Time-of-Arrival (ToA) of coronal mass ejections (CME) at Earth is a key parameter due to the space weather phenomena associated with the CME arrival, such as intense geomagnetic storms. Several approaches to estimate the ToA based on kinematical parameters derived from single- and multi-viewpoint white-light coronagraph observations have been proposed and implemented, particularly in the last decade. Despite the incremental use of new instrumentation and the development of novel methodologies, ToA estimated errors remain above 10 hours on average. Here, we investigate the prediction of ToA of CMEs using observations solely from heliospheric imagers, i.e., from heliocentric distances higher than those covered by the existent coronagraphs. To that aim, we analyse 14 CMEs observed by the heliospheric imager HI-1 onboard the twin STEREO spacecraft to determine their front location and speed. Outside the field of view of the instruments, we assume that the dynamics of the CME evolution is controlled by the aerodynamic drag, a force that comes from the interaction with particles from the background solar wind. We found a CME ToA error mean value of 0.4 ± 7.3 hours ToA and a mean absolute error of 6.1 ± 3.6 hours in a set of 14 events. The results we found here illustrate that observations from HI-1 allow us to estimate the ToA with similar errors than observations from coronagraphs.

1 Introduction

Coronal mass ejections (CMEs) have been tracked with space-based coronagraphs for more than 40 years. Thousands of events have been studied and cataloged (Tousey, 1973; Gosling et al., 1974; Robbrecht & Berghmans, 2004; Yashiro, 2004; Vourlidas et al., 2017). One of the key open issues about CMEs is understanding their propagation in the heliosphere, specially for events directed to Earth.

CMEs are the main drivers of intense geomagnetic storms (Gosling, 1993) and one of the most basic variables from a Space Weather perspective is the Time-of-Arrival (ToA) of a given CME in the Earth's vicinity. Not surprisingly, the ToA has been studied for a long time. An extensive review of methods to estimate the ToA and their results can be found in Zhao and Dryer (2014) and Vourlidas et al. (2019).

The methods applied to ToA estimation include empirical approaches, magneto-hydrodynamic (MHD) modeling, CME three dimensional (3D) reconstruction, and CME propagation analysis based on drag-based models, just to name a few (see, e.g., Zhao and Dryer (2014)). In

spite of the insight gained with the dual view-point provided by the Solar Terrestrial Relations Observatory (STEREO) mission (Kaiser et al., 2007) since 2007, the uncertainty of the CME ToA persist. According to Vourlidas et al. (2019), the average CME ToA accuracy is 9.8 ± 2 hours. The identification of the source of these errors is not straightforward. The evaluation and comparison of the different methodologies across the literature is complicated because of the different event samples, assumptions with regard to the propagation of the events in the interplanetary medium (i.e., beyond the field of view of the instrument utilized), and ToA criteria. Hence, it is difficult to asses which methodology yields the best results, i.e., the lowest ToA error. In general, the errors tend to be lower for small samples studies, which is most likely due to an event-selection bias.

Thanks to the Sun-Earth Connection Coronal and Heliospheric Investigation (SECCHI) suite onboard STEREO, CMEs can be observed further into the inner heliosphere by the heliospheric imagers (HI-1 and HI-2). Details about SECCHI are described in R. A. Howard et al. (2008). Nevertheless, a quick check of the literature reveals that the use of the imaging products of the heliospheric imagers is limited compared to those of the coronagraphs (Vourlidas et al., 2019; Zhao & Dryer, 2014).

The relative contribution of the electron corona signal (i.e., the K-corona) to the total signal recorded by the HI instruments for elongations greater than about 8° ($\sim 32\ R_\odot$) is well below that recorded by coronagraphs, all of them covering smaller heliocentric distances. Therefore, to help reveal the CME boundaries and inner structure during their evolution across the HI instrument field-of-view (FOV), it is necessary to remove the dominant signal coming from the F-corona, i.e., photospheric light scattered by the dust particles in orbit around the Sun (Leinert et al., 1998).

In addition, at the solar elongation covered by the heliospheric imagers, the emission properties of the coronal electrons change due to Thomson Scattering (Minnaert, 1930). The maximum brightness contribution along the line of sight is now located on the "curved" Thomson sphere rather than the flat "sky-plane" (Vourlidas and Howard (2006) and references therein). This effect complicates the visualization of the event boundaries, as CMEs move away from the Sun.

To help reveal the faint K-coronal structures in STEREO HI-1 FOV, Stenborg and Howard (2017) devised an algorithm to model the background signal (a proxy of the F-corona) out of each individual image. The technique exploits the break out in spatial

frequencies between the discrete K-corona structures and the smooth and homogeneous F-corona signal. In this work, we take advantage of this state-of-the-art methodology to investigate the effect of a cleaner identification of the CME boundaries to higher heliocentric distances in the estimation of the ToA at Earth.

To carry out the investigation, we apply a customized version of the technique developed by Stenborg and Howard (2017) to remove the background signal in the HI-1 FOV on a set of 14 Earth-directed CME events spread over the rise and maximum of Cycle 24 (2010-2013). Co-temporal HI-1 observations from two viewpoints are used to construct an elliptical model of the CME fronts and hence estimate their locations in the solar corona. Beyond the HI-1 FOV, we apply a drag force model to propagate the CME up to 1 au. We finally compare the CME ToA errors computed with this approach to those calculated using mainly observations from SECCHI coronagraphs.

A motivation for this work is the application of similar methodology to CME observations in the inner heliosphere from upcoming and planned missions, such as the recently selected PUNCH or L5-mission concepts (Lavraud et al., 2016).

This article is organized as follows. In Section 2.1 we describe the events studied. From Section 2.2 to Section 2.8, we describe the methodology applied to calculate the CME kinematics in the HI-1 FOV and extrapolate them in the remaining trajectory toward the Earth. The results (the calculated CME travel time, final speed, etc.) and a comparison with the actual observations are shown in Section 3. Finally, we summarize the results in Section 4.

2 Materials and Methods

We devised a methodology to estimate the CME ToA by combining a geometric front reconstruction model with a CME propagation model. To obtain the CME propagation direction, we fit the CME front in the ecliptic plane with an ellipse (see Section 2.5). To determine the CME kinematics, we use an aerodynamic drag force model (see Section 2.6). The elliptical front allows us to estimate the initial position and the speed, which are then used as input parameters for the drag force estimation. As a final result, we derive the CME speed and ToA at 1 au.

2.1 Event List

Our starting point is the list of CME events analyzed by Sachdeva et al. (2017), which includes 38 well-observed events between March 2010 and March 2013. Since our study is targeting only observations from heliospheric imagers, we do not use the kinematic parameters and height-time profiles derived by Sachdeva et al. (2017) because they were derived using observation from coronagraphs (SECCHI and LASCO) and heliospheric imagers. We take only the timing of each event to identify the corresponding observations on the HI-1 FOV. Moreover, Sachdeva et al. (2017) did not identify the CME counterparts in the Earth's vicinity (the so-called interplanetary coronal mass ejections - ICMEs); therefore, we undertake this task for each event.

For this task, we use the ICME list compiled from WIND mission observations from Nieves-Chinchilla et al. (2018), which is available online at `https://wind.nasa.gov/ICMEindex.php`. Our criterion to associate a given ICME to its corresponding CME counterpart is based on the time elapsed (t_{el}) between the ICME in situ observation time and the time of the first coronagraph observation of the CME counterpart candidate. The CME travel time considered was taken from an extensive study of CME-ICMEs pairs by Richardson and Cane (2010). We consider it a match when 0.5 days $< t_{el} <$ 5 days.

From our initial list comprising 38 events (Table 1) we could identify 30 ICMEs counterparts. The 8 unmatched events are #7, #10, #12, #14, #15, #16, #22 and #23 (indicated by $\emptyset$ in column "Remark"). In these cases, either the corresponding ICME was not included in the ICME list possibly due to data gaps or poor data quality, or the CME reported on Sachdeva et al. (2017) missed the WIND spacecraft.

In two other cases (#8 and #32, rows labeled "too short" in Table 1), the ICME event arrives at Earth less than 24 hours after the time of first appearance in the coronagraph FOV as reported in Sachdeva et al. (2017) in spite of the very low speed reported for this CME event. For other event (#35, row labeled "too long"), the travel time is longer than 5 days and hence it is not considered to be a reasonable CME-ICME pair. Since we have not made a comprehensive study of all other CMEs observed in close timing to each of our events (few days before and after and including other instruments from the SECCHI suite or from LASCO coronagraphs C2 and C3), some of the three ICME with unreasonable travel time are perhaps not associated to the CMEs under study. We considered that these CME-ICME association are inconsistent and removed them from our analysis.

Table 1. List of CMEs and corresponding ICMEs. The symbols ‖ indicate the events removed from the list due to observation of another CMEs in close timing. Events associated to multiple ICMEs, without any ICME associated, or whose time elapsed between the CME and corresponding ICME observation falls outside our criteria are indicated by Π, ∅ and Δ, respectively. We could not apply the F-corona background removal methodology (see Section 2.2) to events indicated by † and they were removed from the analysis. The final list of 14 events that match all the criteria explained in Section 2.1 and that could be processed as explained in Section 2.2 are indicated by a star.

ID	Remark	Date	Realistic timing	Unique ICME	ICME start date
1	†	2010/03/19	yes	yes	2010/03/23 22:29
2	⋆	2010/04/03	yes	yes	2010/04/05 07:55
3	⋆	2010/04/08	yes	yes	2010/04/11 12:20
4	‖	2010/06/16	yes	yes	2010/06/21 03:35
5	†	2010/09/11	yes	yes	2010/09/15 02:24
6	†	2010/10/26	yes	yes	2010/10/31 02:29
7	∅	2010/12/23	-	-	-
8	Δ	2011/01/24	Too short	yes	2011/01/24 06:43
9	⋆	2011/02/15	yes	yes	2011/02/18 19:50
10	∅	2011/03/03	-	-	-
11	⋆	2011/03/25	yes	yes	2011/03/29 09:07
12	∅	2011/04/08	-	-	-
13	⋆	2011/06/14	yes	yes	2011/06/17 02:09
14	∅	2011/06/21	-	-	-
15	∅	2011/07/09	-	-	-
16	∅	2011/08/04	-	-	-
17	⋆	2011/09/13	yes	yes	2011/09/17 02:57
18	‖	2011/10/22	yes	yes	2011/10/24 17:41
19	‖	2011/10/26	yes	yes	2011/11/01 08:09
20	‖	2011/10/27	yes	yes	2011/11/02 00:21
21	Π	2012/01/19	yes	no	2012/01/21 04:02
22	∅	2012/01/23	-	-	-
23	∅	2012/01/27	-	-	-
24	†	2012/03/13	yes	yes	2012/03/15 12:35
25	⋆	2012/04/19	yes	yes	2012/04/23 02:15
26	⋆	2012/06/14	yes	yes	2012/06/16 09:03
27	⋆	2012/07/12	yes	yes	2012/07/14 17:39
28	⋆	2012/09/28	yes	yes	2012/09/30 10:14
29	⋆	2012/10/05	yes	yes	2012/10/08 04:12
30	⋆	2012/10/27	yes	yes	2012/10/31 14:28
31	‖	2012/11/09	yes	yes	2012/11/12 22:12
32	Δ	2012/11/23	Too short	yes	2012/11/23 20:51
33	⋆	2013/03/15	yes	yes	2013/03/17 05:21
34	⋆	2013/04/11	yes	yes	2013/04/13 22:13
35	Δ	2013/06/28	Too long	yes	2013/07/04 17:17
36	Π	2013/09/29	yes	no	2013/10/02 01:15
37	†	2013/11/07	yes	yes	2013/11/08 21:07
38	†	2013/12/07	yes	yes	2013/12/08 07:31

In two particular cases (events #21 and #36, indicated by Π in column "Remark" of Table 1), there is more than one ICME candidate. These events were also removed from our analysis because it is impossible to confirm (at least with the data we are using in the current analysis) which ICME corresponds to the CME arrival.

We also removed CME events from the list of Sachdeva et al. (2017) that were preceded or followed closely (within less than 24 hours) by other CME events. We performed this analysis on HI-1 FOV only (both on STEREO-A and STEREO-B) and considered the timing of the first observation of each event. These events are removed from the travel time analysis because interaction between consecutive is likely CMEs before their arrival at 1 au. Five events fit this criterion (#4, #18, #19, #20 and #31) and are indicated by ‖ in column "Remarks" of Table 1. When CME-CME interaction takes places, a detailed study would be necessary because additional forces need to be taken into account in the CME propagation to estimate their travel time (see, e.g., Liu et al. (2012); Colaninno et al. (2013); Temmer et al. (2012), just to name a few). Case studies of CME interaction are beyond the scope of the present manuscript.

Therefore, from the original list of 38 events, 20 were left after the application of all criteria mentioned in the paragraphs above.

2.2 Removal of the background F-corona

The HI-1 observations include a background scene that must be removed to allow the CME event characterization by analysing the K-corona emission. This background scene is dominated by the scattering from dust particles in orbit around the Sun, the so-called F-corona (the F letter stands for Fraunhofer). The F-corona intensity overtakes the K-corona above approximately $5R_{\odot}$ (Koutchmy & Lamy, 1985), well below the inner edge of the HI-1 instrument, which is about $16R_{\odot}$.

Experience from observations of the corona over the last 40 years suggests that the F-corona is constant over timescales of days or weeks while the K-corona is highly dynamic and can change significantly in a matter of hours. For this reason, empirical models of the F-corona are usually constructed by computing the minimum of the daily median images over an extended period of time (normally a solar rotation), centered on the day of observation (Morrill et al., 2006).

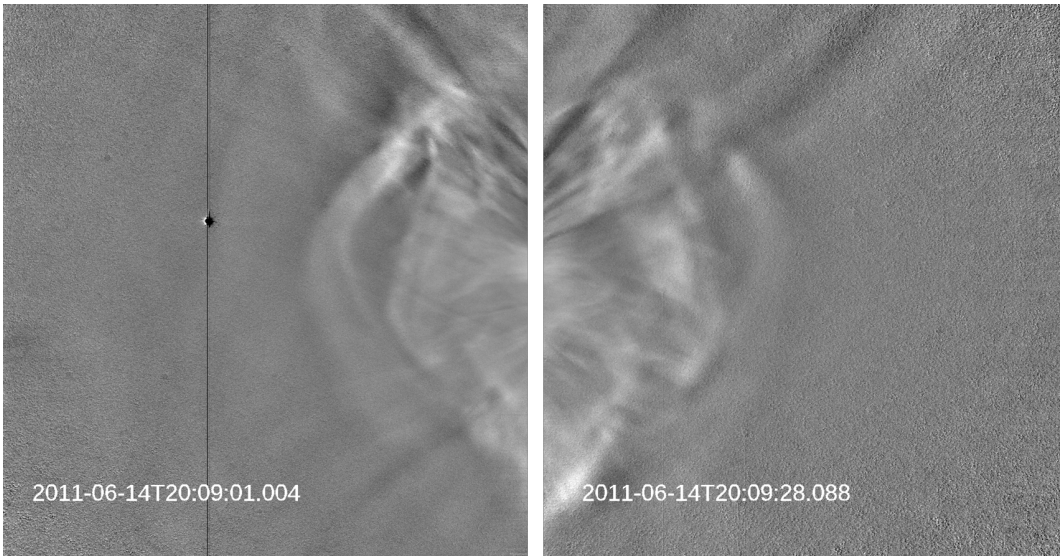

Figure 1. Example of CME #13 (2011/06/14) observed on HI-1-A (left) and HI-1-B (right) FOVs after removal of the background F-corona.

Stenborg and Howard (2017) showed that at the larger elongations covered by the HI-1 instruments, the use of background models obtained considering extended periods of time leads to the introduction of artifacts. This occurs due to the subtle changes resulting form different viewpoints (Stenborg et al., 2018). Therefore, to remove the background contribution from the F-corona from each individual HI-1 observation, we created its respective background model following Stenborg and Howard (2017).

An example of a processed HI-1 observation pair highlighting a CME feature is shown in Figure 1. The resulting images shown in this figure clearly reveal the morphology of both the CME front and the internal structures without the known artifacts that result from the use of the running difference scheme generally adopted by the solar physics community. In the current study, we focused on the selection of the CME furthermost point visible in the HI-1 FOV at each time-instance and at a position angle close to the ecliptic plane. Since we are interested in the arrival of the transient at the Earth, we did not take any measurement of their internal structure (e.g., the core of the events).

As mentioned above, for some events in Table 1, the corresponding observations could not be properly processed (i.e., the background brightness model could not be determined) due to the presence of extended bright objects in the FOV of the instruments (e.g., the Milky Way), saturated objects (e.g., a bright planet) and/or instrumental artifacts (e.g.,

ghost features). We kept only events with simultaneous observation in HI-1 both on-board STEREO-A and STEREO-B that allowed proper identification of the CME front in at least part of the FOV in each spacecraft. Due to these reasons, the following 6 events were removed from our analysis: #1, #5, #6, #24, #37 and #38. After removing these 6 events from the 20 available after the application of criteria explained in Section 2.1, we end up having 14 events.

2.3 Extraction of the elongation profiles

To analyze the kinematic evolution of the events, we need to identify their corresponding fronts in the processed images and construct elongation-time maps of a given part of the fronts. The spatial location can then be derived under some assumptions for translating angular positions to heliocentric distances.

Given a set of sequential images observed by HI-1, we selected a position angle (PA) close to the ecliptic plane to construct the time-elongation profiles, frequently called J-maps (Davies et al., 2009). We use the PA of 90° for STEREO-A and 270° for STEREO-B, a region that nearly corresponds to the central height of the image. The PA is kept constant for a given CME event in each viewpoint, i.e., it is set to be the same at all instances. Each time-elongation profile constructed in this way shows at least one bright feature that looks like an inclined line. This corresponds to the brighter points along the selected PA in the images, i.e., to the apex of the CME projected onto the plane of the sky at that particular PA. An example of a J-map created for event #1 is shown in Figure 2. Note that the brighter tracks in the map appear surrounded by a darker region. This is just a result of the image processing applied to the images to reveal the CME features, which exploits the brightness contrast between the foreground and background in a way resembling an unsharp mask filter.

Once the J-map is created, we select the front by eye. Since the identification is subjective, we repeat this procedure 9 times so that we can have an estimate of the error associated to the identification by eye. In the following steps we normally take 3 time-elongation profiles: the median, minimum and maximum for each time instance (hereafter $\epsilon_{med}[t]$, $\epsilon_{min}[t]$, $\epsilon_{max}[t]$). These 3 profiles are all used to estimate the CME Time-of-Arrival (ToA) at Earth, as described in Section 2.5 and Section 3.

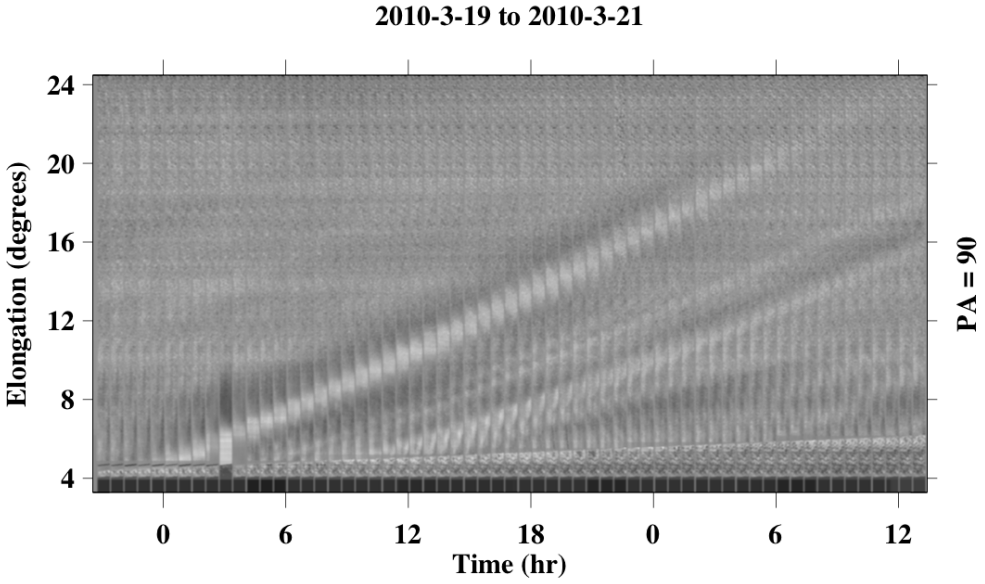

Figure 2. Example of J-map of CME #1 (2010/03/19) observed on HI-1-A FOV

In a few events, the J-maps produced at the PA mentioned (90° for STEREO-A and 270° for STEREO-B) were not clear and we used PA shifted by up to 3 degrees instead. This happened due to the presence of artifacts in the background at a given elongation, such as a bright planet. This negatively affected the CME front tracking in the J-map at that particular PA due to the excessive brightness of this feature as compared to that of both the background and the CME front. From our assessment using a few test CMEs, we understood that the shifted position angle within the range mentioned here produces differences that are within the error range between (from ϵ_{min} to ϵ_{max}) and, therefore, are not expected to affect significantly the results found here.

2.4 Overview of the CME Time-of-Arrival and Speed-on-Arrival determination

We calculate the travel time and Speed-on-Arrival of the CME using the drag model (Section 2.6) and kinematic parameters derived only from HI-1 observations from both spacecraft.

The delineation of the procedure followed is depicted in the diagram in Figure 3. Briefly, we first extract the elongation of the CME front at a given PA as a function of time inde-

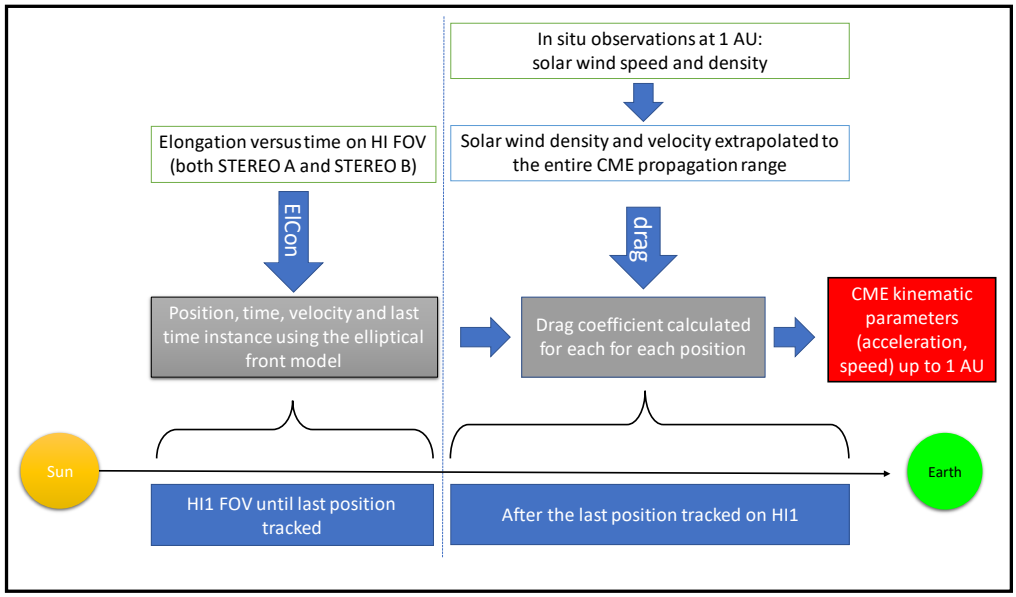

Figure 3. Diagram explaining the CME's Time-of-Arrival (ToA) and Speed-on-Arrival (SoA) determinations. The left half illustrates the determination of CME front as a function of time from observation in the HI-1 FOV. The right half explains the application of the drag model, that is used only after the last position observed on HI-1 FOV. The boxes in white indicate inputs for the models and their outputs are shown in gray. The blue boxes indicate the range (along the Sun-Earth line) where each methodology is applied.

pendently for each telescope. Then, a geometric model (Section 2.5) is used to derive the CME front position at each time instance, as well as its direction of propagation and its speed. These parameters are then used to calculate the CME acceleration at each point (in steps of 0.01 au along the Sun-Earth line) after its last observation on HI-1 (typically from tenths of solar radii) to the L1 point (around 220 $R_{\odot}$) using the aerodynamic drag model (Section 2.6).

We have not considered other forces, such as the Lorentz force in this model, because this force is considered to be important only closer to the Sun, especially for fast CMEs (Sachdeva et al., 2015, 2017).

2.5 The elliptical front model

To derive the CME position in the HI-1 FOV, we adopt the Elliptical Conversion (ElCon) model as described in Möstl et al. (2015) and Rollett et al. (2016). This model

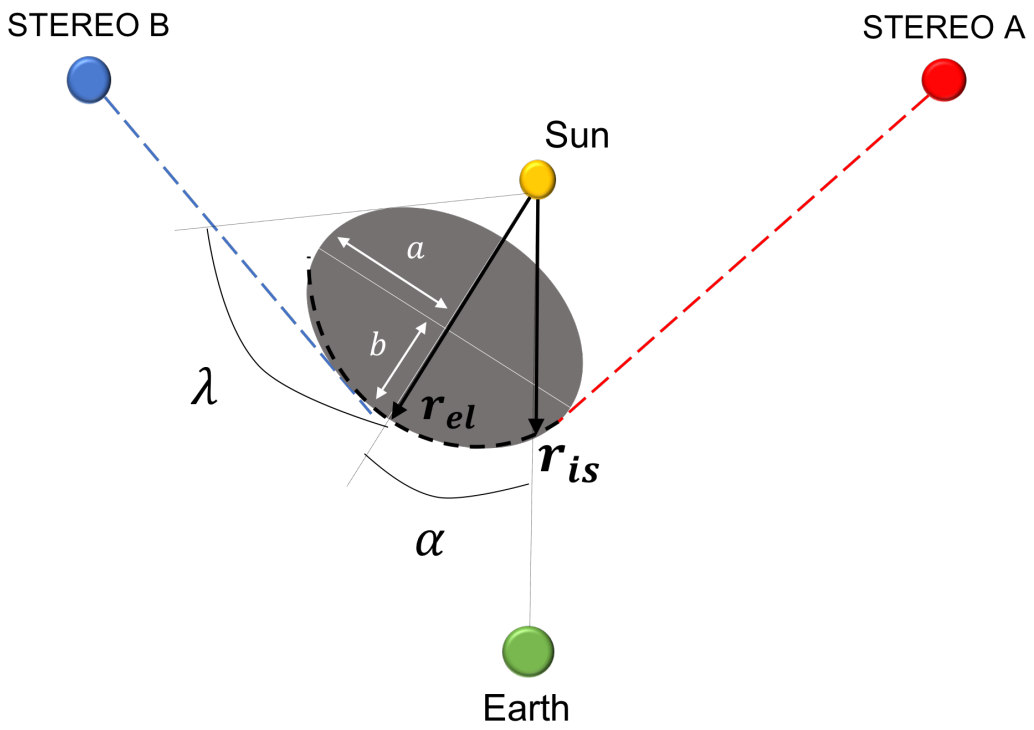

Figure 4. The elliptical front model used in this study to derive the CME front position (dashed black line). The parameters of the model (CME half width in the ecliptic plane λ, aspect ratio of elliptical front $f = a/b$, central position angle in the ecliptic plane α) are derived by a best-fit of a sequence of time-instances observed simultaneously by HI-1-A and HI-1-B. For each time-instance we derive the position of the CME front point along the Sun-Earth line (r_{is}) and along the central axis of the CME (r_{el}).

considers an elliptically shaped CME front on the ecliptic plane. Its position and speed can then be derived at any location in space using just geometrical arguments, provided the time evolution of the front's elongation is known and a set of given parameters of the CME front (e.g., angular width, direction of propagation, aspect ratio, etc.) are defined. The model adds an extra degree of freedom when compared to cylindrical CME fronts. Since the CMEs can have various shapes, the elliptical front should be a good fit for more events. This model and its parameters are shown in Figure 4.

In this study, we derive the parameters of the model (CME half width in the ecliptic plane λ, aspect ratio of elliptical front f, central position angle in the ecliptic plane α, speed) by doing a best-fit of a sequence of n time-instances observed simultaneously by

HI-1-A and HI-1-B. In previous studies these parameters were fixed for a given set of CMEs for simplicity (Möstl et al., 2015; Rollett et al., 2016). The residual σ was calculated from the following expression:

$$\sigma = \sum_{t=1}^{n} (|r_{is}(t)^A - r_{is}(t)^B| + |r_{el}(t)^A - r_{el}(t)^B|)/n$$

where $r_{is}(t)$ is the position of the CME front point along the Sun-Earth line on the ecliptic plane as a function of time, t, derived using observations from a given spacecraft; $r_{el}(t)$ denotes the position of the central axis on the CME front. The angle between r_{is} and r_{el} corresponds to α. Positive values of α indicate that the CME propagates towards STEREO-A. The superscripts A and B indicate values from STEREO-A and STEREO-B observations, respectively.

The list of parameters derived using the ElCon model is shown in Table 2. As already mentioned, from the list of 38 events shown in Table 1, only 14 are used with the ElCon model. The rest were removed due to the reasons described in Section 2.1 and 2.2.

We have fit the elliptical model three times for each event: one using the median elongation extracted at each time instance $\epsilon_{med}[t]$, a second with minimum elongation $\epsilon_{min}[t]$ and a third time using the maximum $\epsilon_{max}[t]$. In each case, a set of parameters λ, f, α is derived and r_{is} at each time instance t is calculated as the average of r_{is}^A and r_{is}^B.

v_{med}, v_{min}, v_{max} are the linear speeds calculated from the parameters of the ElCon derived using $\epsilon_{med}[t]$, $\epsilon_{min}[t]$ and $\epsilon_{max}[t]$, respectively. All three speeds considered here are calculated along the Sun-Earh line, i.e., using r_{is}. The difference between the 3 values (typically well below 100 km/s) give us an idea of the error introduced in the CME speed due to differences in the identification of the CME front in the J-maps. The 3 speeds are used for the calculation of the CME travel time and ToA error, as described in Section 3. The remaining parameters shown in Table 2 (f, λ, σ and α) are calculated using the median elongation profile.

2.6 The drag model

The aerodynamic drag results from the interaction of the CME with the solar wind. There are many references applying such force and most of them rely on empirical drag coefficients (Cargill, 2004; Vršnak, 2006; T. A. Howard et al., 2007; Borgazzi et al., 2009; Byrne

Table 2. Parameters of the CMEs elliptical front derived using the ElCon model: linear speeds (v_{med}, v_{min} and v_{max}), CME half width in the ecliptic plane (λ), aspect ratio of the front (f) and the CME central position angle on the ecliptic plane (α, positive ahead of the Earth). Other parameters shown are the residual (σ) and the position of the last point that the CME was tracked simultaneously on both viewpoints (s_0).

ID	last tracked time (UT) (UT)	s_0 [au]	v_{med} [km/s]	v_{min} [km/s]	v_{max} [km/s]	f	λ [°]	σ [au]	α [°]
2	03-Apr-2010 20:29:21	0.22	846	866	876	0.5	80	0.0047	-17
3	09-Apr-2010 00:39:22	0.28	490	448	491	0.6	60	0.0021	12
9	15-Feb-2011 18:29:34	0.26	465	456	475	0.5	65	0.0028	-12
11	26-Mar-2011 07:59:25	0.20	448	446	427	0.5	50	0.0033	-11
13	14-Jun-2011 23:49:28	0.28	769	765	775	0.5	70	0.0081	-19
17	14-Sep-2011 10:29:53	0.14	605	584	568	0.5	80	0.0093	63
25	20-Apr-2012 10:29:25	0.25	446	446	453	0.5	80	0.0079	-32
26	15-Jun-2012 03:19:22	0.27	741	755	776	0.5	80	0.0051	-7
27	13-Jul-2012 07:59:27	0.31	743	732	780	0.9	80	0.0475	20
28	28-Sep-2012 08:29:50	0.18	740	721	739	0.6	20	0.0056	20
29	06-Oct-2012 01:49:52	0.36	692	686	712	0.5	30	0.0075	15
30	28-Oct-2012 11:59:57	0.21	431	422	441	0.5	20	0.0097	11
33	15-Mar-2013 15:59:43	0.19	765	703	737	0.6	80	0.0030	1
34	11-Apr-2013 15:49:33	0.18	764	780	667	0.5	65	0.0042	-1

et al., 2010; Maloney & Gallagher, 2010; Vršnak et al., 2010, 2012; Mishra & Srivastava, 2013; Dolei et al., 2014; Iju et al., 2014; Temmer & Nitta, 2015).

Among these works, many authors have used a constant drag coefficient for a given CME in its path from the Sun to the Earth so that the drag could only be a function of: (i) the difference between the CME and solar wind speed, (ii) CME mass, (iii) solar wind density and (iv) cross section area of the CME. Only a few works have used a drag coefficient as a function of the Reynolds number, which in turn depends on the viscosity of the solar wind plasma (Subramanian et al., 2012; Sachdeva et al., 2015). Following Sachdeva et al. (2015), we consider the drag force description given by:

$$F_{drag}[s] = -m_{CME}\ \gamma[s]\ (v_{CME}[s] - v_{SW}[s])\ |v_{CME}[s] - v_{SW}[s]|,$$

where v_{CME} is the CME speed and v_{SW} is the background solar wind speed. Both speeds are a function of CME position s along the Sun-Earth line. For a CME propagating towards the Earth, s increases as time passes. m_{CME} is the CME mass taken from the CDAW CME catalog (Yashiro, 2004). If not available, we consider $m_{CME} = 1.1 \times 10^{15} g$, the median value reported on Vourlidas et al. (2010) for CMEs observed between 1996 and 2009. γ is given by:

$$\gamma\,[s] = C_D\,[s]\,n_{SW}\,[s]\,\frac{m_P A_{CME}[s]}{m_{CME}}$$

where C_D is the dimensionless drag parameter, n_{SW} is the solar wind proton number density, m_P is the proton mass, A_{CME} is the CME cross section area (explained in the next paragraphs) and m_{CME} is the CME mass. Typically γ has values range from $1 \times 10^{-9}\ km^{-1}$ to $2 \times 10^{-7}\ km^{-1}$, see, e.g. Temmer and Nitta (2015) and Vršnak et al. (2013).

In several previous studies, C_D was empirically determined while considered to be constant (see, e.g. Cargill (2004); Vršnak et al. (2010); Mishra and Srivastava (2013); Temmer and Nitta (2015), and references therein). In these studies, C_D typically ranges from 0.2 to 0.4.

In this study, on the other hand, we determine the value of C_D using a set of equations based on a physical definition of the CME aerodynamic drag introduced by Subramanian et al. (2012) and previously studied by Sachdeva et al. (2015, 2017). Here we describe C_D using the following expression determined experimentally by Achenbach (1972):

$$C_D\,[s] = 0.148 - 4.3 \times 10^4 (Re\,[s])^{-1} + 9.8 \times 10^{-9} Re[s]\ .$$

This equation for C_D is a fit to data observed on a solid metal sphere immersed on a flow with high Reynolds number Re. We considered that this result is suitable for the interaction of the CME with the background solar wind because (i) the equation of the drag force considers a solid-like body immersed on a high-Reynolds number and (ii) typically the boundaries of magnetic clouds (and therefore, CMEs) are over-pressured structures that do not tend to deform in response to tangential stresses because the total pressure (magnetic plus plasma) has a substantial jump in this region according to Jian et al. (2006).

The Reynolds number depends on the macroscopic lenghtscale of the CME, its velocity relative to the background solar wind particles and the viscosity of the solar wind. For more details, the reader is referred to Sachdeva et al. (2017).

The CME cross section area A_{CME} is calculated as:

$$A_{CME}\,[s] = \pi \times \; R^2_{CME}\,[s] \times w/360$$

where w is the width of the CME (in degrees, as determined by the CME CDAW catalog) and R_{CME} is the radius of the CME that was taken to be $0.4s$. This expression of R_{CME} was experimentally chosen in this study as a good solution to reduce the ToA error for the set of CME events studied here among different values of the coefficient lower than the unit.

2.7 Background solar wind speed

As described in previous section, the solar wind speed v_{SW} at any point along the Sun-Earth is required to calculate the drag. Close to 1 au, the solar wind conditions are continuously observed by instrumentation at the Lagrangian point L1, such as by the Solar Wind Electron, Proton, and Alpha Monitor (SWEPAM) instrument (McComas et al., 1998) onboard Advanced Composition Explorer (ACE) mission (Stone et al., 1998) and by the Solar Wind Electron (SWE) instrument (Ogilvie et al., 1995) onboard Wind spacecraft (King, 2005). In the remaining points of the trajectory, on the other hand, v_{SW} need to be calculated using empirical models or simulation.

In this study, we use an empirical expression to extrapolate the solar wind speed at any position along the Sun-Earth line using observation at 1 au ($v_{SW@1au}$). Following N. R. Sheeley et al. (1997) and Sheeley et al. (1999), the solar wind speed along the Sun-Earth line ($v_{sw}[s]$) is considered to be:

$$v_{SW}[s] = v_{SW@1au}[1 - e^{-(s-r_0)/r_a}]$$

where s is a given position along the Sun-Earth line, $r_0 = 1.5\ R_\odot$ is the distance from the Sun where the solar wind is taken to be zero and $r_a = 50\ R_\odot$ is the distance over which the asymptotic speed is reached. According to this model, the solar wind speed increases more significantly close to the Sun, typically up to approximately 100 $R_\odot$, and then it is almost constant up to 1 au.

In this work, we considered that $v_{SW@1au}$ is the average observed value in the time period from 48 up to 24 hours before the CME first observation on LASCO C2. We chose this time period taking into account the typical travel time for a solar wind packet to travel from the solar corona to 1 au.

2.8 Background solar wind density

Besides the solar wind speed, the solar wind density along the CME trajectory is also required for calculating the drag force as described in Section 2.6. Again, the observations are limited to 1 au and the density evolution must be derived via a model. The solar wind proton density n_{SW} as a function of position s is given by

$$n_{SW}[s] = \left(\frac{n_{SW@1au}}{7.2}\right)\left(3.3 \times 10^5 s^{-2} + 4.1 \times 10^6 s^{-4} + 8 \times 10^7 s^{-6}\right)$$

where $n_{SW@1au}$ is the solar wind density observed in the L1 Lagrangian Point (close to 1 au). Here we use the model of electron density from Leblanc et al. (1998) assuming that the electron and proton densities are equal. The term between parentheses considers the difference of the density at 1 au from the original value of 7.2 cm^{-3} used on the model. $n_{SW@1au}$ was assumed to be the average observation value from 48 up to 24 hours before the CME first observation on LASCO C2.

3 Results

3.1 Application of the drag model

We use the position of the CME at the time of the last HI-1 observation in the calculation of the drag coefficient and the linear speed of the portion of the CME front along the Sun-Earth line (v_{med}, v_{min}, v_{max}). Some geometric parameters derived using ElCon (such as the angular width and angle) are not used directly by the drag force, but they are indirectly taken into account in the derivation of r_{is} in each time-instance.

We start the application of the drag model at the last HI-1 observation position (s_0). In some cases, the brightness of the CME front is equal to the background and the CME front cannot be resolved, specially in the outer half of the FOV. Thus, the s_0 position changes from event to event, and it is indicated in the second column of Table 2. Typically, the last height-time observation ranges between 20 and 80 solar radii.

An example of the application of the drag model is shown in Figure 5. In each panel, the horizontal axis shows the distance from the Sun (in solar radii). In the top left panel, the black line denotes the acceleration based on the initial speed v_{med}. Acceleration profiles based on v_{min} and v_{max} are indicated by the red and blue lines, respectively. The CME speed derived using v_{med} as initial speed is shown in the second panel, from top to bottom. The speed of the background solar wind speed (v_{sw}) is indicated by the green line. The remaining lines represent speeds calculated using v_{min} and v_{max}. The background solar wind proton density is represented on the third panel, from top to bottom. Other parameters shown are drag coefficient (fourth panel, from top to bottom), the Reynolds number (fifth panel) and the viscosity (lower panel).

For all analyzed events, C_D has a decreasing profile from the Sun to 1 au, typically with steeper slope close to the Sun, as shown in Figure 5. The variations for the different cases arise from differences between the CME and background solar wind speed and density, and the CME area and mass. Close to the Sun, C_D ranges from 0.36 to 0.19 while at L1 its values ranges from 0.16 to 0.28. Values of C_D in any position mentioned above lie in the same range than previous studies that adopted a single drag coefficient for a set of events, which have values typically chosen between 0.2 and 0.4.

As the CME moves toward the Earth, the background solar wind speed increases asymptotically. Given the nature of the drag force, the CME decelerates and, as a result, the magnitude of the drag force decreases. Other reasons for the decrease in the drag force with distance are: (i) the solar wind density (n_{sw}) decreases (from values typically around 50 cm^{-3} to 5 cm^{-3} and/or (ii) the Reynolds number (Re) decreases thus reducing the drag coefficient C_D.

All 14 CMEs in our sample decelerate since all have $v_{CME} > v_{SW}$. The deceleration rate is higher close to the Sun (values up to 3.25 m/s^2) and decreases as the CME propagates toward 1 au.

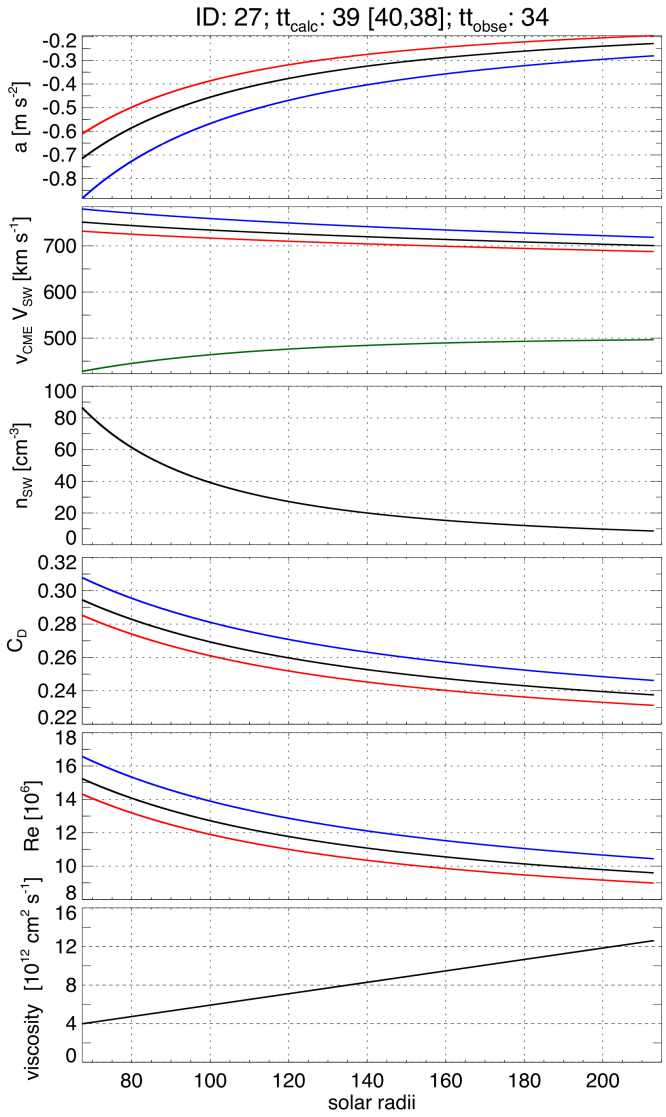

Figure 5. The application of the drag force to a sample CME that is decelerated from the solar corona to 1 au. In the panels with multiple lines, the black ones indicate the CME kinematic parameters calculated using v_{med} and the red and blue lines indicate CME parameters calculated using v_{min} and v_{max}, respectively. The green line on the second panel (from top to bottom) indicates the background solar wind speed.

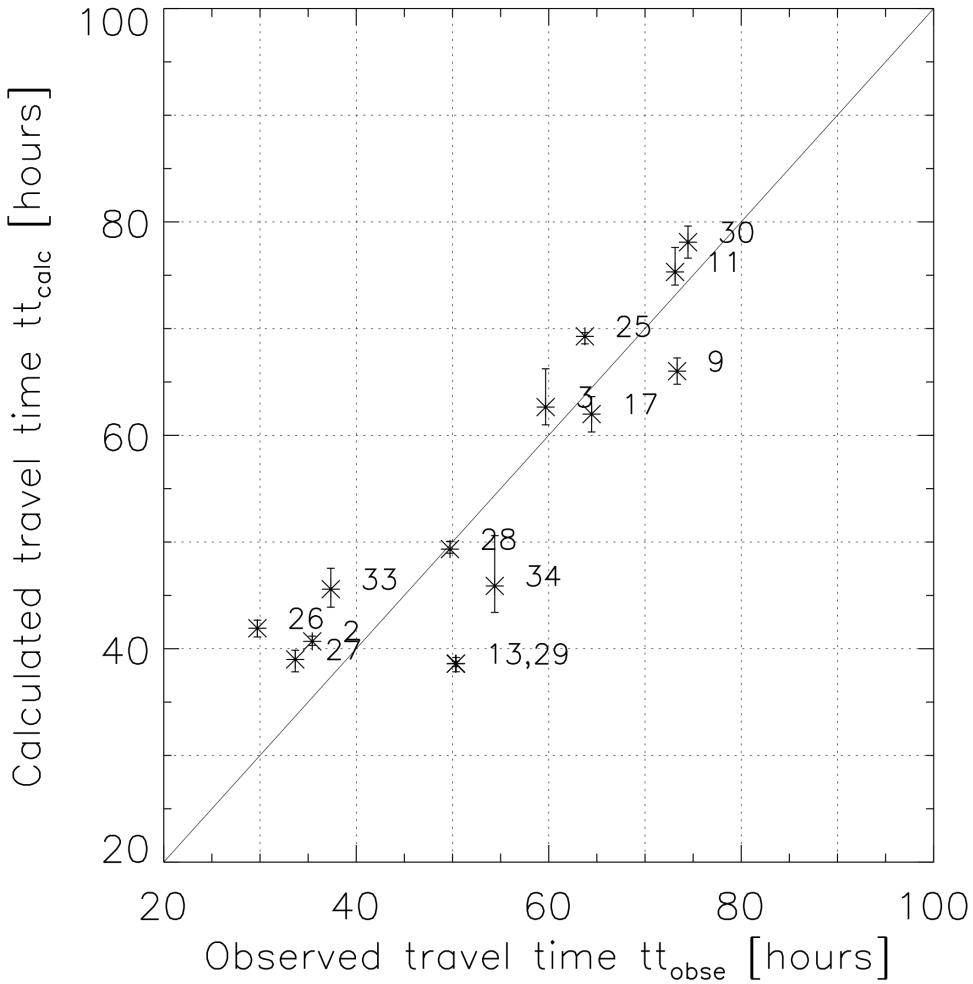

Figure 6. The calculated and observed travel time (from the last observation on HI-1 FOV until L1). The labels correspond to the CME IDs in Table 1. The line indicates the points where the model and observed travel times are identical, i.e., the ToA error is zero ($\delta t = 0$).

3.2 The CME Time-of-Arrival (ToA) errors

In this section we compare the CME travel time from its last HI-1 observation point s_0 up to 1 au calculated using the aerodynamic drag model (tt_{calc}) with the actual travel time (tt_{obse}). The latter is the time difference between the first ICME observation and the last CME observation at s_0. The results are shown in Figure 6.

The instant of the CME arrival at Earth is clearly identified from in situ observations for all events studied here. All events are preceded by a clear discontinuity in the magnetic field

and solar wind parameters (solar wind speed, density and temperature). For this reason, it is unlikely that the CME ToA errors found here are due to by ambiguous determination of ICME arrival time. Since tt_{obse} is not expected to be a source of errors, we focus this study on sources of errors associated to tt_{calc}.

For the 14 CME-ICMEs pairs studied here, the ToA error mean value is 0.4 ± 7.3 hours and the mean absolute error (MAE) is 6.1 ± 3.6 hours. The Pearson correlation coefficient found when we compare tt_{calc} and t_{obs} is 0.87.

According to an extensive review of CME ToA from Vourlidas et al. (2019) that considers more than 20 studies of ToA error, the MAE found here lies among the lowest values. Among the previous studies, 7 consider the drag force (most of them using empirical values of γ rather than the model we adopted here) and only one adopted the ElCon model (although without using simultaneous observations from STEREO). Our sample size is among the smallest (only 14 CMEs are analyzed): other studies using drag-based model included up to 34 events and other references about empirical methods have more than 200 CMEs in their sample. The main reasons for the small data set are our rather strong selection criteria. As mentioned in Section 2.1, we require simultaneous observations from both HI-1s, events well-separated in time/space and reliable CME-ICME identifications.

The relatively low ToA error found here does not necessarily mean that the methodology is better than in studies with higher MAE and larger event sizes. However, it is an encouraging indication that better ToA estimates could be attained via carefully selected event samples along with improved image processing and measurements higher in the corona (when the CME is more likely to be in equilibrium with its surroundings)

Our results along with results from Rollett et al. (2016), suggest that the HI-1 leads to lower ToA error than coronagraph observation, at least among those reported on Vourlidas et al. (2019). This suggests that the observations from HI-1 are suitable for CME ToA estimates at least for the set of events analyzed here.

3.3 The CME Speed-on-Arrival (SoA) and its error

In this section we compare the CME Speed-on-Arrival (SoA) at 1 au derived from our drag-based model with the corresponding in situ observed ICME speed (v_{ICME}).

Table 3. Calculated and observed CME travel time and speed between end HI-1 FOV and L1.

ID	first observation (UT)	last tracking (UT)	Arrival at 1 au (UT)	tt_{calc} $[h]$	tt_{obse} $[h]$	δt $[h]$	v_{init} $[km/s]$	v_{final} $[km/s]$	v^{+}_{final} $[km/s]$	v^{-}_{final} $[km/s]$	v_{ICME} $[km/s]$	$v_{SW@1au}$ $[km/s]$	$n_{SW@1au}$ $[cm^{-3}]$
2	03-Apr-2010 10:33:58	03-Apr-2010 20:29:21	05-Apr-2010 07:55:00	41	35	6	863	752	757	746	666	620	4
3	08-Apr-2010 04:54:07	09-Apr-2010 00:39:22	11-Apr-2010 12:20:00	63	60	3	476	466	478	443	419	401	5
9	15-Feb-2011 02:24:05	15-Feb-2011 18:29:34	18-Feb-2011 19:50:00	66	73	-7	465	456	464	448	487	378	5
11	25-Mar-2011 08:48:25	26-Mar-2011 07:59:25	29-Mar-2011 09:07:00	75	73	2	440	436	443	423	361	346	5
13	14-Jun-2011 06:12:05	14-Jun-2011 23:49:28	17-Jun-2011 02:09:00	39	50	-11	770	756	761	752	458	448	5
17	14-Sep-2011 00:00:05	14-Sep-2011 10:29:53	17-Sep-2011 02:57:00	62	64	-2	586	558	572	546	463	455	5
25	19-Apr-2012 15:12:09	20-Apr-2012 10:29:25	23-Apr-2012 02:15:00	69	64	5	448	445	450	443	377	340	5
26	14-Jun-2012 14:12:07	15-Jun-2012 03:19:22	16-Jun-2012 09:03:00	42	30	12	757	676	687	666	431	408	10
27	12-Jul-2012 16:48:05	13-Jul-2012 07:59:27	14-Jul-2012 17:39:00	39	34	5	752	701	719	688	590	500	9
28	28-Sep-2012 00:12:05	28-Sep-2012 08:29:50	30-Sep-2012 10:14:00	49	50	-1	733	639	643	630	345	279	5
29	05-Oct-2012 02:48:05	06-Oct-2012 01:49:52	08-Oct-2012 04:12:00	39	50	-11	697	659	672	650	377	323	5
30	27-Oct-2012 16:48:05	28-Oct-2012 11:59:57	31-Oct-2012 14:28:00	78	74	4	431	405	412	399	354	279	5
33	15-Mar-2013 07:12:05	15-Mar-2013 15:59:43	17-Mar-2013 05:21:00	46	37	9	735	721	747	693	625	536	5
34	11-Apr-2013 07:24:06	11-Apr-2013 15:49:33	13-Apr-2013 22:13:00	46	54	-8	737	728	769	661	482	421	2

manuscript submitted to *JGR: Space Physics*

In this study, we calculated the SoA in 3 different ways for each CME, labelled v_{final}, v^{-}_{final} and v^{+}_{final} (Table 3). They were calculated using v_{med}, v_{min} and v_{max}, respectively, as initial speeds in the drag model. The difference between v_{med}, v_{min} and v_{max} comes from the multiple visual CME identification in the J-map (as described in Section 2.3) and it is $< 50\ km\ s^{-1}$ for all events, except for #34 that is 113 $km\ s^{-1}$. For all events in our list, the mean value of $v^{+}_{final} - v^{-}_{final}$ is 28 $km\ s^{-1}$. Compared to the typical CME speed error, which is about 100 $km\ s^{-1}$ (Mierla et al., 2010), the errors found in this study can be considered low.

This result illustrates that the specific feature selected on a given J-map by eye (responsible for the difference in the initial speed used on the drag model) leads to a minor difference on the SoA. An example of CME speeds as a function of position calculated using both v_{min} and v_{max} is shown in Figure 5 (second panel, from top). They are represented by the blue and red lines, respectively. In this example the difference between v^{-}_{final} and v^{+}_{final} is 31 $km\ s^{-1}$.

The ICME speed v_{ICME} is calculated here as the average proton speed observed in situ during the ICME period reported on the Wind ICME list. The data used here comes from the OMNI database and consists of merged observations from the ACE and the Wind spacecraft.

The distribution of v_{final} versus v_{ICME} is shown in Figure 7. The error bars shown in the plot are defined by v^{+}_{final} and v^{-}_{final}. The CME SoA error ($\delta v = v_{final} - v_{ICME}$) is $140 \pm 109\ km\ s^{-1}$ and the SoA MAE is $144 \pm 102\ km\ s^{-1}$. The trend is that the CME arrival speed calculated here is higher than the actual ICME speed. The Pearson correlation coefficient between v_{final} and v_{ICME} is 0.60, lower than the correlation found comparing observed and calculated travel times.

The SoA error is not reduced significantly when we consider v^{+}_{final} and v^{-}_{final}. This indicates that the error in the initial CME speed, estimated via multiple visual identifications on the J-maps, cannot explain the majority of the SoA error. In this way, this error could be due to (i) an error in the initial CME speed (v_{init}) due to the ElCon model and its assumptions, such as linear speed and fixed direction of propagation; (ii) an incomplete or incorrect description of the forces that affect the CME propagation from s_0 to 1 au; and/or (iii) the v_{ICME} does not correspond to the CME front speed precisely. This could happens because v_{ICME} is measured in situ from observations of the solar wind particles around

the observing spacecraft and v_{final} is a parameter describing the CME front as a whole, having dimensions that are orders of magnitude larger than the region observed in situ by a spacecraft.

The SoA MAE was compared with results from 5 other studies, as shown in Table 1 of Vourlidas et al. (2019). Our results are similar except the much lower SoA in Rollett et al. (2016) ($16 \pm 53\ km\ s^{-1}$).

We identified that 5 events studied here (# 13, #26, #28, #29 and #34) have SoA absolute error ($|\delta v| = |v_{final} - v_{ICME}|$) higher than 200 $km\ s^{-1}$ while the remaining are lower than 120 $km\ s^{-1}$ (this can be seen clearly in Figure 7. We tried to identify any trend between the $|\delta v|$ and input parameters used in the drag model, particularly those that change between events. We could not find, though, any trend between $|\delta v|$ and CME mass, width, background solar wind speed in the corona and 1 au nor solar wind density at 1 au.

One common point among events with higher $|\delta v|$ is that the CME initial speed is between $\sim 700\ km\ s^{-1}$ and $\sim 800\ km\ s^{-1}$. The opposite is not true, however. Some CMEs with initial speed in the same range have $|\delta v|$ among the lowest values ($<\ 120\ km\ s^{-1}$).

3.4 CME ToA and SoA errors during different background solar wind conditions

In this section we discuss whether the aerodynamic drag model adopted here lead to δt and δv higher or lower in any particular condition of the background solar wind condition, such as proton density or speed.

The drag force, according to the description in Section 2.6, depends on the difference between CME and background solar wind speed. Our events occur over a diverse range of 1 au solar wind speeds, $v_{sw@1au}$, as listed in the second column of Table 3, from right to left. Since $v_{sw@1au}$ is used to extrapolate the solar wind speed to s_0, it affects the drag force in the whole range calculated here.

In all cases studied here we observed that the v_{sw} is lower than v_{CME} at the first point of application of the drag force (s_0) and, as a result, the drag force produces deceleration. In 11 of the 14 events studied here, $v_{sw@1au}$ was lower than 500 km/s. The highest value of $v_{sw@1au}$ was observed in CME #2: 620 km/s. In some events (such as #28 and #30), the solar wind speed is particularly low $v_{sw@1au} = 279\ km/s$.

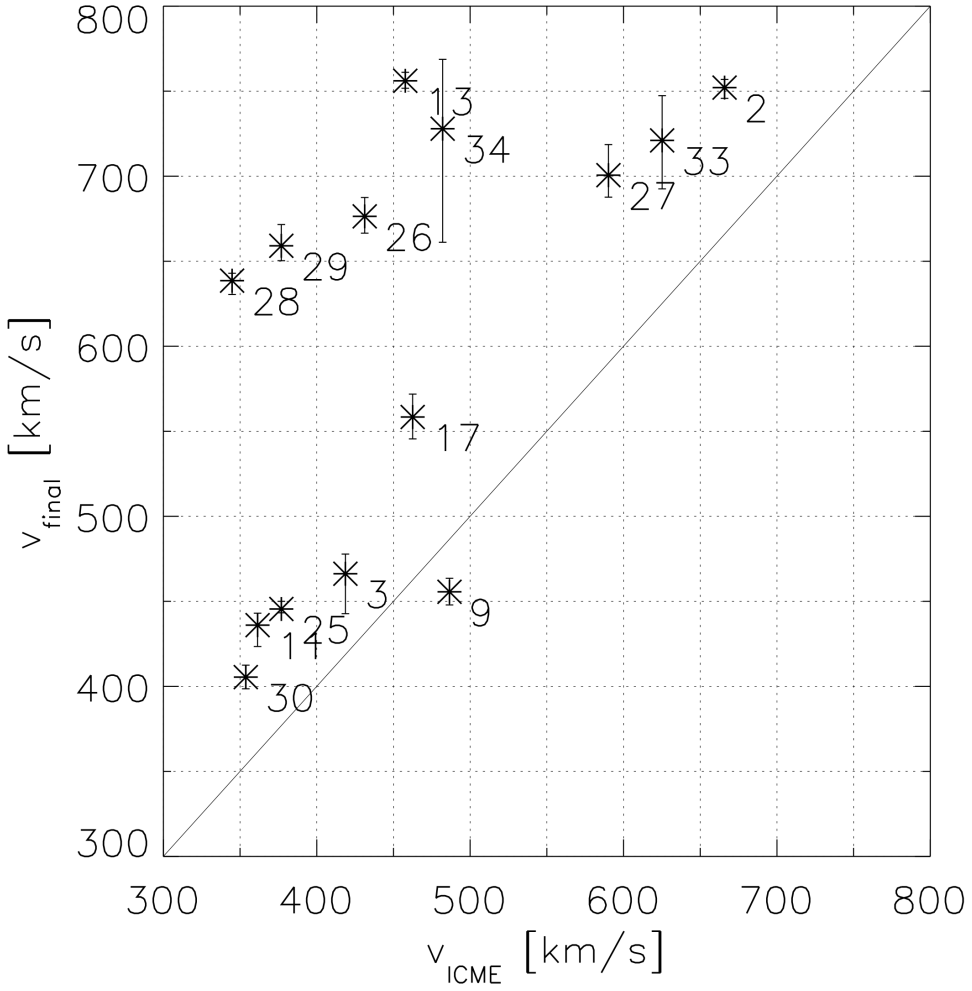

Figure 7. The CME speed calculated at 1 au using the drag model (v_{final}) compared to the in situ ICME speed (v_{ICME}). The labels correspond to the CME IDs in Table 1. The line represents the region with $\delta v = 0$, i.e., the position a given event would be located if it had null SoA error.

When comparing v_{sw} to δt or δv, we did not find any clear trend. This result can be interpreted in two alternative ways: (a) the drag force description used here leads to similar errors in any background solar wind speed values or (b) δt and δv found here are mainly associated to sources other than the drag force, such as errors in the determination of initial CME speed, direction of propagation or position.

Other observed solar wind parameter used in the drag model is the background solar wind density at 1 au. This is used to estimate the solar wind density at any position along the path used on the drag force calculation. Among the set of events studied here, the solar wind density is higher than the average for quiet periods ($n_{SW@1au} = 5\ cm^{-3}$) only in two events (#26 and #27). In these cases, $n_{SW@1au}$ is approximately two times higher than the quiet period values.

We did not see any trend when associating the background solar wind density with the δt and δv errors. This result suggests that the drag model usability is not limited to average values of solar wind density since the errors found are not clearly different in any background solar wind density condition observed in the cases studied here.

3.5 The contribution of the drag force on the CME SoA estimation

The CME speed variation ($\Delta v = v_{final} - v_{init}$) in the entire range we applied the drag force (from s_0 up to 1 au) is $> 100\ km\ s^{-1}$ for event #2 and $\Delta v\ >\ 50\ km\ s^{-1}$ for the following events: #26, #27 and #28. On the remaining 10 events, $0\ <\ \Delta v\ <\ 50\ km\ s^{-1}$.

Since the typical error of CME speed in coronagraph observations is around $100\ km\ s^{-1}$ (Mierla et al., 2010), we conclude that the contribution of the drag force on the SoA is small and within the error range of the CME speed observations, at least for the events considered here and within the heights we apply the drag force (from s_0 up to 1 au). Here s_0 ranges from 0.14 au (32 solar radii) to 0.36 au (77 solar radii).

Our results agree with Sachdeva et al. (2015) who found that the drag force is minimum at distances above 15-50 solar radii for slow CMEs since they propagate almost at constant speeds after that range.

A second point is that all events with $\Delta v\ > 50\ km\ s^{-1}$ have $v_{init}\ >\ 697\ km\ s^{-1}$ but some events with $v_{init} > 697\ km\ s^{-1}$ (#13, #33 and #34) have $\Delta v\ <\ 30\ km\ s^{-1}$. This result illustrate that although the drag force absolute value is frequently higher for

high-speed CMEs, this force is also strongly affected by other factors in some events studied here.

3.6 The contribution of the aerodynamic drag force on the CME ToA estimation

In order to assess the importance of the drag force in the estimation of the ToA, we repeated its calculation ignoring the drag force. This corresponds to a very simplified model consisting of a CME propagating from s_0 (located in the HI-1 FOV) to 1 au with constant speed equals to the initial speed attributed to the CME v_{init} after applying the ElCon model.

The ToA mean error found considering no drag force is -1.2 ± 7.0 h and ToA mean absolute error is 5.8 ± 3.9 h. Comparing these values to the results found using the drag force, we can see that they are slightly higher but still within the error range.

This result suggests that the contribution of the drag force is at most at the same level of magnitude than other unknown reasons that could explain the ToA error. As discussed in Section 3.5, results from previous studies using the same drag force model suggest that this is not very expressive at the position range that s_0 typically lies.

We do not understand that this means, necessarily, that the drag model should be considered negligible for studying CME propagation. The drag force is normally more intense at points closer to the Sun than at the position studied here (s_0) because the solar wind speed is lower and, at least for fast CMEs, the CME speed is higher. Both factors result in higher drag forces in positions closer to the Sun than studied here and lead to higher ToA error when aerodynamic drag force is simply neglected.

3.7 Does Tracking the CME further in the HI-1 FOV reduces ToA and SoA errors?

The application of the drag model used here does not start at the same position for all 14 events analyzed. Each CME is tracked until s_0, which is the last point where it is clearly observed in HI-1 FOV (onboard both STEREO-A and STEREO-B). After this, the drag is applied from this point up to 1 au, as explained in Section 2.4. CMEs with lower s_0 have their speed, direction of propagation and morphological parameters (such as angular width

in the ecliptic plane and elliptical aspect ratio) derived in a smaller position range along the Sun-Earth line and drag force application starts closer to the Sun.

In the set of 14 events analyzed here, there is no correlation between the SoA absolute error $|\delta v| = |v_{final} - v_{ICME}|$ and s_0. There is, however, a trend that CME with higher s_0 have higher absolute values of ToA errors $|\delta t|$.

The trends observed here could arise from the following considerations: (i) as a CME moves away from the Sun, its brightness decreases in the HI-1 FOV and identifying its front becomes more ambiguous; (ii) errors associated to the ElCon assumptions about CME kinematics. As described in Section 2.5, we are assuming linear speed and fixed direction of propagation for each CME up to s_0 when we are deriving its parameters using ElCon. After s_0, a free parameter for acceleration is included but the direction propagation is still assumed to be constant.

The last hypothesis for higher $|\delta t|$ is also pointed out on Barnard et al. (2017). The authors observed unrealistic acceleration in regions close to the outer side of the HI-1 FOV, mainly after typical values of s_0. The same study also found unrealistic accelerations when other methods with constraints in the direction of propagation were used, such as harmonic mean and self-similar expansion. In this way, results from Barnard et al. (2017) seem to support hypothesis (ii) as the explanation for higher $|\delta t|$ found is found in events with higher s_0 studied here.

4 Conclusions

Starting with a list of 38 Earth-directed CMEs in 2010-2013 compiled by Sachdeva et al. (2017), we reduced it to 14 events by applying three rather strict criteria: simultaneous observations from both HI-1, clear CME-ICME identifications, and events separated in time to avoid CME-CME interactions. Our objective was to minimize as much as possible the errors in the measurements of the CME kinematics and ToA. The arrival time of all 14 events could be unambiguously determined from in-situ observation thanks to a discontinuity clearly observed in both magnetic field and solar wind plasma parameters.

We extracted the kinematics of the events using solely observations from HI-1 and extrapolated both their time-of- and their speed-on- arrival using a drag force model. The modeled CME speed at 1 au was typically higher than the observed ICME speed. This was the case for all events analyzed but one (#9). SoA absolute errors are higher than 200 km/s

for 5 events (#13, #26, #28, #29 and #34) and below 120 km/s for the remaining 8 events. This suggests that either the actual initial CME speed was lower than what our measurements suggested or that the deceleration magnitude calculated using the drag-based model studied here was lower than the actual one. The latter seems to be a more likely explanation since excess SoA is a common result in many studies (Vourlidas et al., 2019).

The resulting ToA absolute errors are below 10 hours for 11 events rising to 12 hours when considering all 14 events. Our MAE compares favorably against past studies and is encouraging regarding our approach. However, the results are based on a small number of events and the methodology may not necessarily lead to lower ToA when applied to more CMEs. We plan to pursue this further by addressing the various issues we identified below.

Sources of ToA and SoA errors can arise in drag force calculation or in the presence of other unaccounted for forces, such as the Lorentz force. Another source of error may be the assumption of the elliptical conversion model used for the determination of the CME radial position from its elongation, such as fixed direction of propagation and constant speed. Finally, errors on the front identification arise towards the outer FOV of HI-1 as the CME front becomes fainter.

The drag force calculation at any point in the CME trajectory depends on the ambient solar wind density and speed. These conditions can change significantly during CME propagation and unfortunately in-situ observations were available only close to the Earth for the CMEs under study. In this study, both solar wind density and speed were extrapolated using empirical expressions. For this reason, the drag force should be understood as an approximation rather than a precise calculation. More realistic solar wind conditions derived using simulation are out of the scope of the present manuscript and could be part of a future study.

The amplitude of the drag force is stronger close to the Sun when compared to conditions close to the Earth. The reason is twofold: (i) the difference between the solar wind and the CME speeds and (ii) the density profile of the solar wind, which is higher close to the Sun (typically by one order of magnitude at 50 solar radii when compared to L1).

Deceleration was observed in all 14 events since all had initial speeds higher than the solar wind speed at the starting point of the drag force application. This deceleration is more intense close to the Sun, where the background solar wind speed is also lower. The

deceleration reaches values up to $-3.25\ m\ s^{-2}$ close to the Sun and $-0.5\ m\ s^{-2}$ close to the Earth.

Despite the difficulties to track CMEs in the HI-1 FOV due to the presence of the F-corona and reduced CME brightness, the results suggest that the ToA error is similar to many studies based on coronagraph observations, at least for the events discussed here.

The recently (2018) launched Parker Solar Probe (PSP) Mission (Fox et al., 2015) has an imager instrument with comparable elongation range to the HI-1 used. This imager is the Wide-field Imager for Solar PRobe (WISPR) (Vourlidas et al., 2016). Similar observations will also be performed by the Solar Orbiter Heliospheric Imager (SoloHI) (R. A. Howard et al., 2019), onboard the upcoming Solar Orbiter (SO) mission (Müller et al., 2013). In this sense, the present study, which relies only on observations from heliospheric imagers, can be used as a guideline for future studies with the PSP and SO targeted on CME ToA or SoA estimations. We hope the results of CME ToA errors estimated could motivate future studies with similar objectives using observations from WISPR and SoloHI.

Acknowledgments

C.R.B. acknowledges grants #2014/24711-6 and #2017/21270-7 from São Paulo Research Foundation (FAPESP). A.V. is supported by NRL N00173-16-1-G029 and NASA NNX16AH70G grants. G.S. and C.R.B. acknowledge the support from the NASA STEREO/SECCHI (NNG17PP27I) program. E.E. acknowledges grants #2018/21657-1 from São Paulo Research Foundation (FAPESP) and #302583/2015-7 from CNPq/PQ. A.D.L acknowledges grant #309916/2018-6 from CNPq/PQ.

The Large Angle Spectrometric Coronagraph instrument (LASCO) was constructed by a consortium consisting of the Naval Research Laboratory (Washington DC, USA), the Max Planck Institute for Solar System Research (currently in Gottingen, Germany, formerly known as the Max Planck Institute for Aeronomie in Kathenburg, Lindau, Germany), the Laboratoire d'Astronomie Spatiale (Marseille, France), and the Space Research Group at the University of Birmingham (Birmingham, UK). LASCO is one of a complement of instruments on the Solar Heliospheric Observatory satellite (SOHO) built in an international collaboration between the European Space Agency (ESA) and National Aero-

nautics and Space Administration (NASA). LASCO data are available for download at `https://lasco-www.nrl.navy.mil/index.php?p=content/retrieve/products`

The SOHO LASCO CME catalog is generated and maintained at the CDAW Data Center by NASA and The Catholic University of America in cooperation with the Naval Research Laboratory. This catalog is available at `https://cdaw.gsfc.nasa.gov/CME_list/`

The Sun Earth Connection Coronal and Heliospheric Investigation (SECCHI) was produced by an international consortium of the Naval Research Laboratory (USA), Lockheed Martin Solar nd Astrophysics Lab (USA), NASA Goddard Space Flight Center (USA), Rutherford Appleton Laboratory (UK), University of Birmingham (UK), Max Planck Institute for Solar System Research (Germany), Centre Spatiale de Lige (Belgium), Institut dOptique Theorique et Applique (France), and Institut d'Astrophysique Spatiale (France). STEREO data are available for download at `https://secchi.nrl.navy.mil/`

This research has made use of the Solar Wind Experiment (SWE) and Magnetic Field Investigations (MFI) instrument's data onboard WIND. We thank to the Wind team and the NASA/GSFC's Space Physics Data Facility's CDAWeb service to make the data available. Wind data are available from `https://cdaweb.sci.gsfc.nasa.gov`. The ICME list compiled from WIND mission observations can be found at `https://wind.nasa.gov/ICMEindex.php`.

References

Achenbach, E. (1972, aug). Experiments on the flow past spheres at very high reynolds numbers. *Journal of Fluid Mechanics*, *54*(03), 565. doi: 10.1017/s0022112072000874

Barnard, L. A., de Koning, C. A., Scott, C. J., Owens, M. J., Wilkinson, J., & Davies, J. A. (2017, jun). Testing the current paradigm for space weather prediction with heliospheric imagers. *Space Weather*, *15*(6), 782–803. doi: 10.1002/2017sw001609

Borgazzi, A., Lara, A., Echer, E., & Alves, M. V. (2009, mar). Dynamics of coronal mass ejections in the interplanetary medium. *Astronomy & Astrophysics*, *498*(3), 885–889. doi: 10.1051/0004-6361/200811171

Byrne, J. P., Maloney, S. A., McAteer, R. J., Refojo, J. M., & Gallagher, P. T. (2010, sep). Propagation of an earth-directed coronal mass ejection in three dimensions. *Nature Communications*, *1*(6), 1–8. doi: 10.1038/ncomms1077

Cargill, P. J. (2004, may). On the aerodynamic drag force acting on interplanetary coronal

mass ejections. *Solar Physics*, *221*(1), 135–149. doi: 10.1023/b:sola.0000033366.10725.a2

Colaninno, R. C., Vourlidas, A., & Wu, C. C. (2013, nov). Quantitative comparison of methods for predicting the arrival of coronal mass ejections at earth based on multiview imaging. *Journal of Geophysical Research: Space Physics*, *118*(11), 6866–6879. doi: 10.1002/2013ja019205

Davies, J. A., Harrison, R. A., Rouillard, A. P., Sheeley Jr., N. R., Perry, C. H., Bewsher, D., ... Brown, D. S. (2009). A synoptic view of solar transient evolution in the inner heliosphere using the Heliospheric Imagers on STEREO. *Geophysical Research Letters*, *36*(2). doi: 10.1029/2008GL036182

Dolei, S., Bemporad, A., & Spadaro, D. (2014, feb). Measurements with STEREO/COR1 data of drag forces acting on small-scale blobs falling in the intermediate corona. *Astronomy & Astrophysics*, *562*, A74. doi: 10.1051/0004-6361/201321041

Fox, N. J., Velli, M. C., Bale, S. D., Decker, R., Driesman, A., Howard, R. A., ... Szabo, A. (2015, nov). The Solar Probe Plus Mission: Humanity's first visit to our star. *Space Science Reviews*, *204*(1-4), 7–48. doi: 10.1007/s11214-015-0211-6

Gosling, J. T. (1993, nov). The solar flare myth. *Journal of Geophysical Research: Space Physics*, *98*(A11), 18937–18949. doi: 10.1029/93ja01896

Gosling, J. T., Hildner, E., MacQueen, R. M., Munro, R. H., Poland, A. I., & Ross, C. L. (1974, nov). Mass ejections from the Sun: A view from Skylab. *Journal of Geophysical Research*, *79*(31), 4581–4587. doi: 10.1029/ja079i031p04581

Howard, R. A., Moses, J. D., Vourlidas, A., Newmark, J., Socker, D., Plunkett, S., ... others (2008). Sun Earth Connection Coronal and Heliospheric Investigation (SECCHI). *Space Science Reviews*, *136*(1-4), 67.

Howard, R. A., Vourlidas, A., Colaninno, R., Korendyke, C., Plunkett, S., Carter, M., ... et al (2019, jun). The solar orbiter heliospheric imager (SoloHI). *Astronomy & Astrophysics*. doi: 10.1051/0004-6361/201935202

Howard, T. A., Fry, C. D., Johnston, J. C., & Webb, D. F. (2007, sep). On the evolution of coronal mass ejections in the interplanetary medium. *The Astrophysical Journal*, *667*(1), 610–625. doi: 10.1086/519758

Iju, T., Tokumaru, M., & Fujiki, K. (2014, jan). Kinematic properties of slow ICMEs and an interpretation of a modified drag equation for fast and moderate ICMEs. *Solar Physics*, *289*(6), 2157–2175. doi: 10.1007/s11207-014-0472-3

722 Jian, L., Russell, C. T., Luhmann, J. G., & Skoug, R. M. (2006, nov). Properties of
723 interplanetary coronal mass ejections at one AU during 1995 – 2004. *Solar Physics*,
724 *239*(1-2), 393–436. doi: 10.1007/s11207-006-0133-2

725 Kaiser, M. L., Kucera, T. A., Davila, J. M., Cyr, O. C. S., Guhathakurta, M., & Christian,
726 E. (2007, nov). The STEREO mission: An introduction. *Space Science Reviews*,
727 *136*(1-4), 5–16. doi: 10.1007/s11214-007-9277-0

728 King, J. H. (2005). Solar wind spatial scales in and comparisons of hourly wind and ACE
729 plasma and magnetic field data. *Journal of Geophysical Research*, *110*(A2). doi:
730 10.1029/2004ja010649

731 Koutchmy, S., & Lamy, P. (1985). The F-Corona and the circum-solar dust evidences
732 and properties [G. Nikolsky Memorial Lecture]. *International Astronomical Union*
733 *Colloquium*, *85*, 6374. doi: 10.1017/S0252921100084359

734 Lavraud, B., Liu, Y., Segura, K., He, J., Qin, G., Temmer, M., ... Fernndez, J. G. (2016,
735 August). A small mission concept to the Sun-Earth Lagrangian L5 point for innovative
736 solar, heliospheric and space weather science. *Journal of Atmospheric and Solar-*
737 *Terrestrial Physics*, *146*, 171–185. doi: 10.1016/j.jastp.2016.06.004

738 Leblanc, Y., Dulk, G. A., & Bougeret, J.-L. (1998). Tracing the electron density from the
739 corona to 1 au. *Solar Physics*, *183*(1), 165–180. doi: 10.1023/a:1005049730506

740 Leinert, C., Bowyer, S., Haikala, L. K., Hanner, M. S., Hauser, M. G., Levasseur-
741 Regourd, A.-C., ... Witt, A. N. (1998, jan). The 1997 reference of diffuse night
742 sky brightness. *Astronomy and Astrophysics Supplement Series*, *127*(1), 1–99. doi:
743 10.1051/aas:1998105

744 Liu, Y. D., Luhmann, J. G., Mstl, C., Martinez-Oliveros, J. C., Bale, S. D., Lin, R. P.,
745 ... Odstrcil, D. (2012, jan). Interactions between coronal mass ejections viewed in
746 coordinated imaging and in situ observations. *The Astrophysical Journal*, *746*(2), L15.
747 doi: 10.1088/2041-8205/746/2/l15

748 Maloney, S. A., & Gallagher, P. T. (2010, nov). Solar wind drag and the kinematics of
749 interplanetary coronal mass ejections. *The Astrophysical Journal*, *724*(2), L127–L132.
750 doi: 10.1088/2041-8205/724/2/l127

751 McComas, D., Bame, S., Barker, P., Feldman, W., Phillips, J., Riley, P., & Griffee,
752 J. (1998, Jul 01). Solar Wind Electron Proton Alpha Monitor (SWEPAM) for
753 the Advanced Composition Explorer. *Space Science Reviews*, *86*(1), 563–612. doi:
754 10.1023/A:1005040232597

Mierla, M., Inhester, B., Antunes, A., Boursier, Y., Byrne, J. P., Colaninno, R., ... Zhukov, A. N. (2010). On the 3-d reconstruction of coronal mass ejections using coronagraph data. *Annales Geophysicae*, *28*(1), 203–215. doi: 10.5194/angeo-28-203-2010

Minnaert, M. (1930, Jan). On the continuous spectrum of the corona and its polarisation. With 3 figures. (Received July 30, 1930). *Zeitschrift fuer Astrophysik*, *1*, 209.

Mishra, W., & Srivastava, N. (2013, jul). Estimating arrival time of earth-directed CMEs at in-situ spacecraft using COR & HI observations from STEREO. *The Astrophysical Journal*, *772*(1), 70. doi: 10.1088/0004-637x/772/1/70

Morrill, J. S., Korendyke, C. M., Brueckner, G. E., Giovane, F., Howard, R. A., Koomen, M., ... Andrews, M. (2006). Calibration of the SOHO/LASCO C3 white light coronagraph. *Solar Physics*, *233*, 331-372. doi: 10.1007/s11207-006-2058-1

Möstl, C., Rollett, T., Frahm, R. A., Liu, Y. D., Long, D. M., Colaninno, R. C., ... Vršnak, B. (2015, may). Strong coronal channelling and interplanetary evolution of a solar storm up to Earth and Mars. *Nature Communications*, *6*(1). doi: 10.1038/ncomms8135

Müller, D., Marsden, R. G., St. Cyr, O. C., Gilbert, H. R., & The Solar Orbiter Team. (2013, Jul 01). Solar orbiter. *Solar Physics*, *285*(1), 25–70. doi: 10.1007/s11207-012-0085-7

Nieves-Chinchilla, T., Vourlidas, A., Raymond, J. C., Linton, M. G., Al-haddad, N., Savani, N. P., ... Hidalgo, M. A. (2018, jan). Understanding the internal magnetic field configurations of ICMEs using more than 20 years of wind observations. *Solar Physics*, *293*(2). doi: 10.1007/s11207-018-1247-z

N. R. Sheeley, J., Wang, Y.-M., Hawley, S. H., Brueckner, G. E., Dere, K. P., Howard, R. A., ... Biesecker, D. A. (1997, jul). Measurements of flow speeds in the corona between 2 and 30r. *The Astrophysical Journal*, *484*(1), 472–478. doi: 10.1086/304338

Ogilvie, K. W., Chornay, D. J., Fritzenreiter, R. J., Hunsaker, F., Keller, J., Lobell, J., ... Gergin, E. (1995, feb). SWE, a comprehensive plasma instrument for the WIND spacecraft. *Space Science Reviews*, *71*(1-4), 55–77. doi: 10.1007/bf00751326

Richardson, I. G., & Cane, H. V. (2010, may). Near-earth interplanetary coronal mass ejections during solar cycle 23 (1996 – 2009): Catalog and summary of properties. *Solar Physics*, *264*(1), 189–237. doi: 10.1007/s11207-010-9568-6

Robbrecht, E., & Berghmans, D. (2004, sep). Automated recognition of coronal mass ejections (CMEs) in near-real-time data. *Astronomy & Astrophysics*, *425*(3), 1097–1106. doi: 10.1051/0004-6361:20041302

Rollett, T., Mstl, C., Isavnin, A., Davies, J. A., Kubicka, M., Amerstorfer, U. V., & Harrison, R. A. (2016, jun). ElEvoHI: a novel CME prediction tool for heliospheric imaging combining an elliptical front with drag-based model fitting. *The Astrophysical Journal*, *824*(2), 131. doi: 10.3847/0004-637x/824/2/131

Sachdeva, N., Subramanian, P., Colaninno, R., & Vourlidas, A. (2015, aug). CME propagation: where does aerodynamic drag "take over"? *The Astrophysical Journal*, *809*(2), 158. doi: 10.1088/0004-637x/809/2/158

Sachdeva, N., Subramanian, P., Vourlidas, A., & Bothmer, V. (2017, aug). CME dynamics using STEREO and LASCO observations: The relative importance of lorentz forces and solar wind drag. *Solar Physics*, *292*(9). doi: 10.1007/s11207-017-1137-9

Sheeley, N. R., Walters, J. H., Wang, Y.-M., & Howard, R. A. (1999, nov). Continuous tracking of coronal outflows: Two kinds of coronal mass ejections. *Journal of Geophysical Research: Space Physics*, *104*(A11), 24739–24767. doi: 10.1029/1999ja900308

Stenborg, G., & Howard, R. A. (2017, apr). A heuristic approach to remove the background intensity on white-light solar images. i.STEREO/HI-1 heliospheric images. *The Astrophysical Journal*, *839*(1), 68. doi: 10.3847/1538-4357/aa6a12

Stenborg, G., Stauffer, J. R., & Howard, R. A. (2018, nov). Evidence for a circumsolar dust ring near mercury's orbit. *The Astrophysical Journal*, *868*(1), 74. doi: 10.3847/1538-4357/aae6cb

Stone, E., Frandsen, A., Mewaldt, R., Christian, E., Margolies, D., Ormes, J., & Snow, F. (1998, Jul 01). The advanced composition explorer. *Space Science Reviews*, *86*(1), 1–22. doi: 10.1023/A:1005082526237

Subramanian, P., Lara, A., & Borgazzi, A. (2012). Can solar wind viscous drag account for coronal mass ejection deceleration? *Geophysical Research Letters*, *39*(19), L19107. (L19107) doi: 10.1029/2012GL053625

Temmer, M., & Nitta, N. V. (2015, jan). Interplanetary propagation behavior of the fast coronal mass ejection on 23 July 2012. *Solar Physics*, *290*(3), 919–932. doi: 10.1007/s11207-014-0642-3

Temmer, M., Vršnak, B., Rollett, T., Bein, B., de Koning, C. A., Liu, Y., ... Forsyth, R. (2012, mar). Characteristics of kinematics of a coronal mass ejection during the 2010 August 1 CME-CME interaction event. *The Astrophysical Journal*, *749*(1), 57. doi: 10.1088/0004-637x/749/1/57

Tousey, R. (1973). The solar corona. In M. J. Rycroft & S. K. Runcorn (Eds.), *Space*

research conference (Vol. 2, p. 713-730).

Vourlidas, A., Balmaceda, L. A., Stenborg, G., & Lago, A. D. (2017, apr). Multi-viewpoint coronal mass ejection catalog based on STEREO COR2 observations. *The Astrophysical Journal*, *838*(2), 141. doi: 10.3847/1538-4357/aa67f0

Vourlidas, A., & Howard, R. A. (2006, may). The proper treatment of coronal mass ejection brightness: A new methodology and implications for observations. *The Astrophysical Journal*, *642*(2), 1216–1221. doi: 10.1086/501122

Vourlidas, A., Howard, R. A., Esfandiari, E., Patsourakos, S., Yashiro, S., & Michalek, G. (2010, sep). Comprehensive analysis of coronal mass ejection mass and energy properties over a full solar cycle. *The Astrophysical Journal*, *722*(2), 1522–1538. doi: 10.1088/0004-637x/722/2/1522

Vourlidas, A., Howard, R. A., Plunkett, S. P., Korendyke, C. M., Thernisien, A. F. R., Wang, D., ... Rodmann, J. (2016, feb). The Wide-Field Imager for Solar Probe Plus (WISPR). *Space Science Reviews*, *204*(1-4), 83–130. doi: 10.1007/s11214-014-0114-y

Vourlidas, A., Patsourakos, S., & Savani, N. P. (2019, jul). Predicting the geoeffective properties of coronal mass ejections: current status, open issues and path forward. *Philosophical Transactions of the Royal Society A: Mathematical, Physical and Engineering Sciences*, *377*(2148), 20180096. doi: 10.1098/rsta.2018.0096

Vršnak, B. (2006, jan). Forces governing coronal mass ejections. *Advances in Space Research*, *38*(3), 431–440. doi: 10.1016/j.asr.2005.03.090

Vršnak, B., Žic, T., Falkenberg, T. V., Mstl, C., Vennerstrom, S., & Vrbanec, D. (2010, mar). The role of aerodynamic drag in propagation of interplanetary coronal mass ejections. *Astronomy and Astrophysics*, *512*, A43. doi: 10.1051/0004-6361/200913482

Vršnak, B., Žic, T., Vrbanec, D., Temmer, M., Rollett, T., Möstl, C., ... Shanmugaraju, A. (2013, Jul 01). Propagation of interplanetary coronal mass ejections: The drag-based model. *Solar Physics*, *285*(1), 295–315. doi: 10.1007/s11207-012-0035-4

Vršnak, B., Žic, T., Vrbanec, D., Temmer, M., Rollett, T., Mstl, C., ... Shanmugaraju, A. (2012, jun). Propagation of interplanetary coronal mass ejections: The drag-based model. *Solar Physics*, *285*(1-2), 295–315. doi: 10.1007/s11207-012-0035-4

Yashiro, S. (2004). A catalog of white light coronal mass ejections observed by the SOHO spacecraft. *Journal of Geophysical Research*, *109*(A7). doi: 10.1029/2003ja010282

Zhao, X., & Dryer, M. (2014). Current status of CME/shock arrival time prediction. *Space Weather*, *12*(7), 448–469. (2014SW001060) doi: 10.1002/2014SW001060

Figure 1.

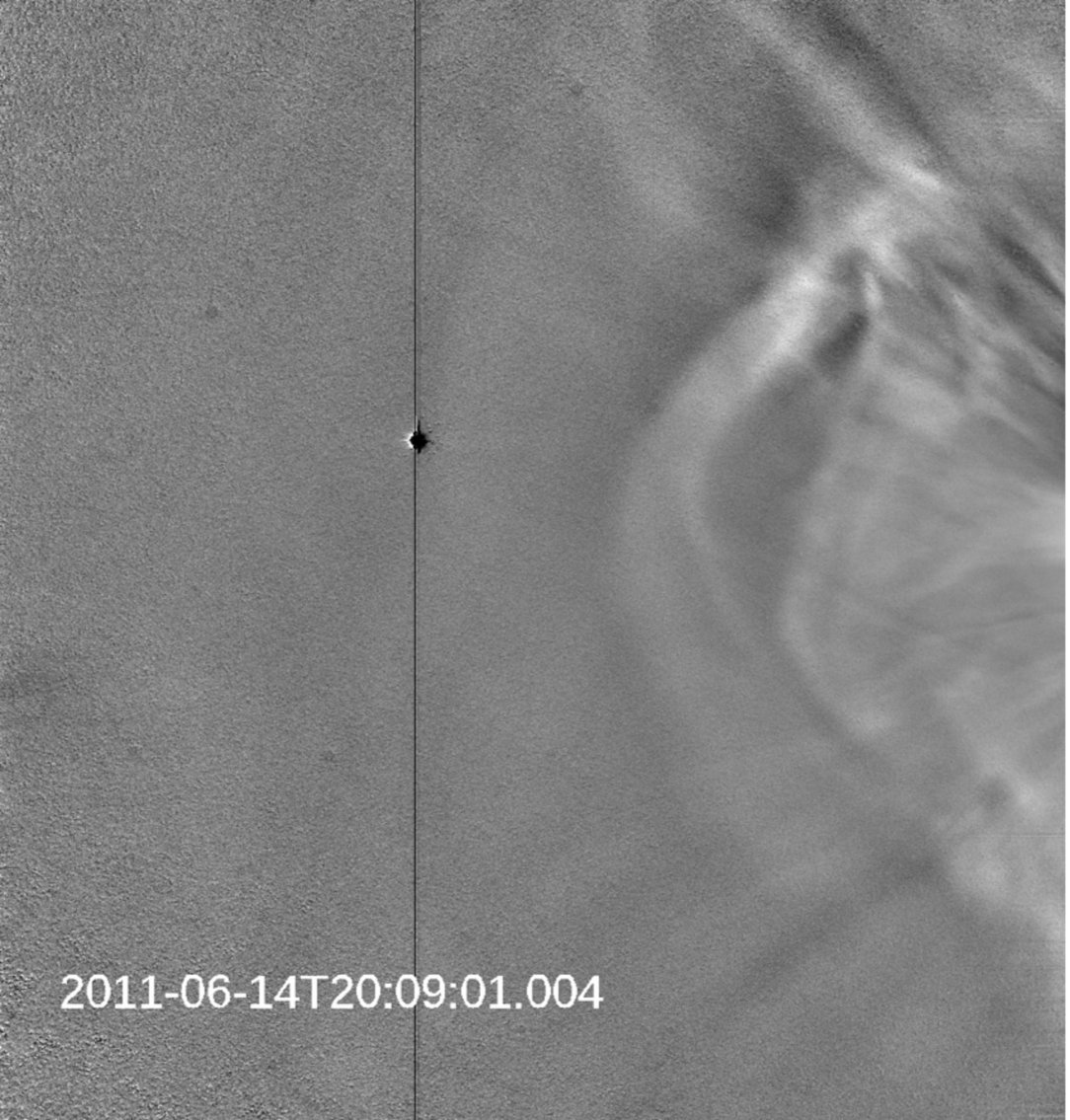
2011-06-14T20:09:01.004

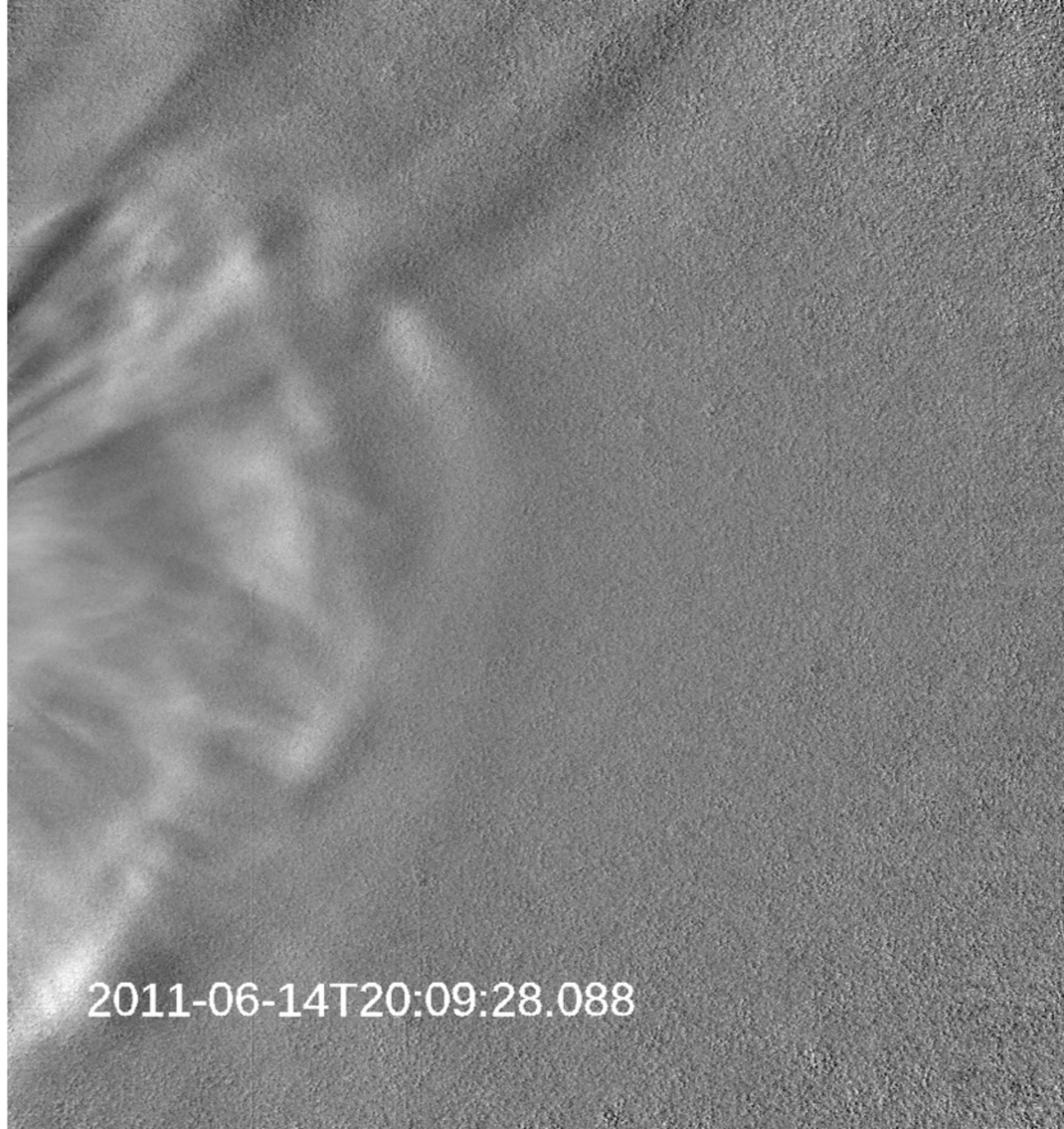
2011-06-14T20:09:28.088

Figure 2.

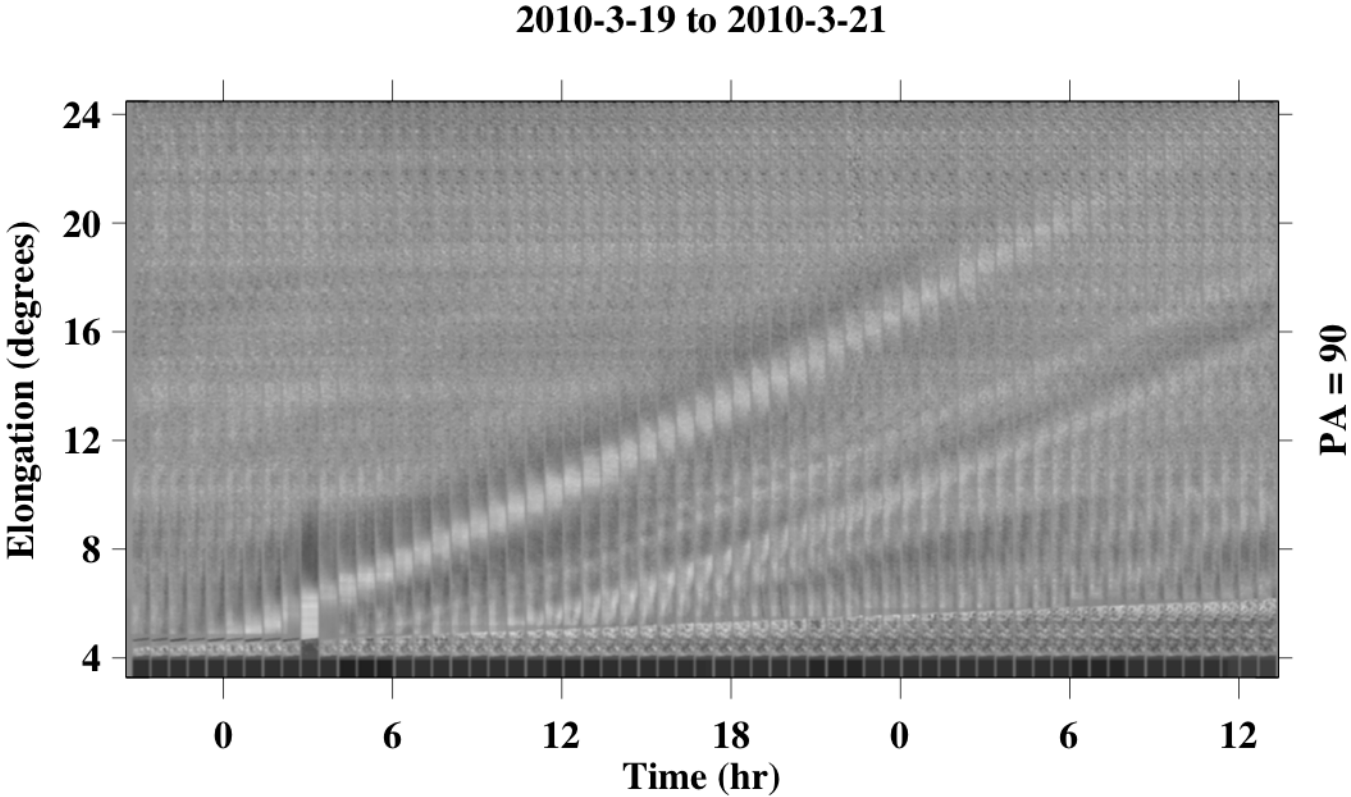
2010-3-19 to 2010-3-21
Elongation (degrees)
24
20
16
12
8
4
0
6
12
18
0
6
12
Time (hr)
PA = 90

Figure 3.

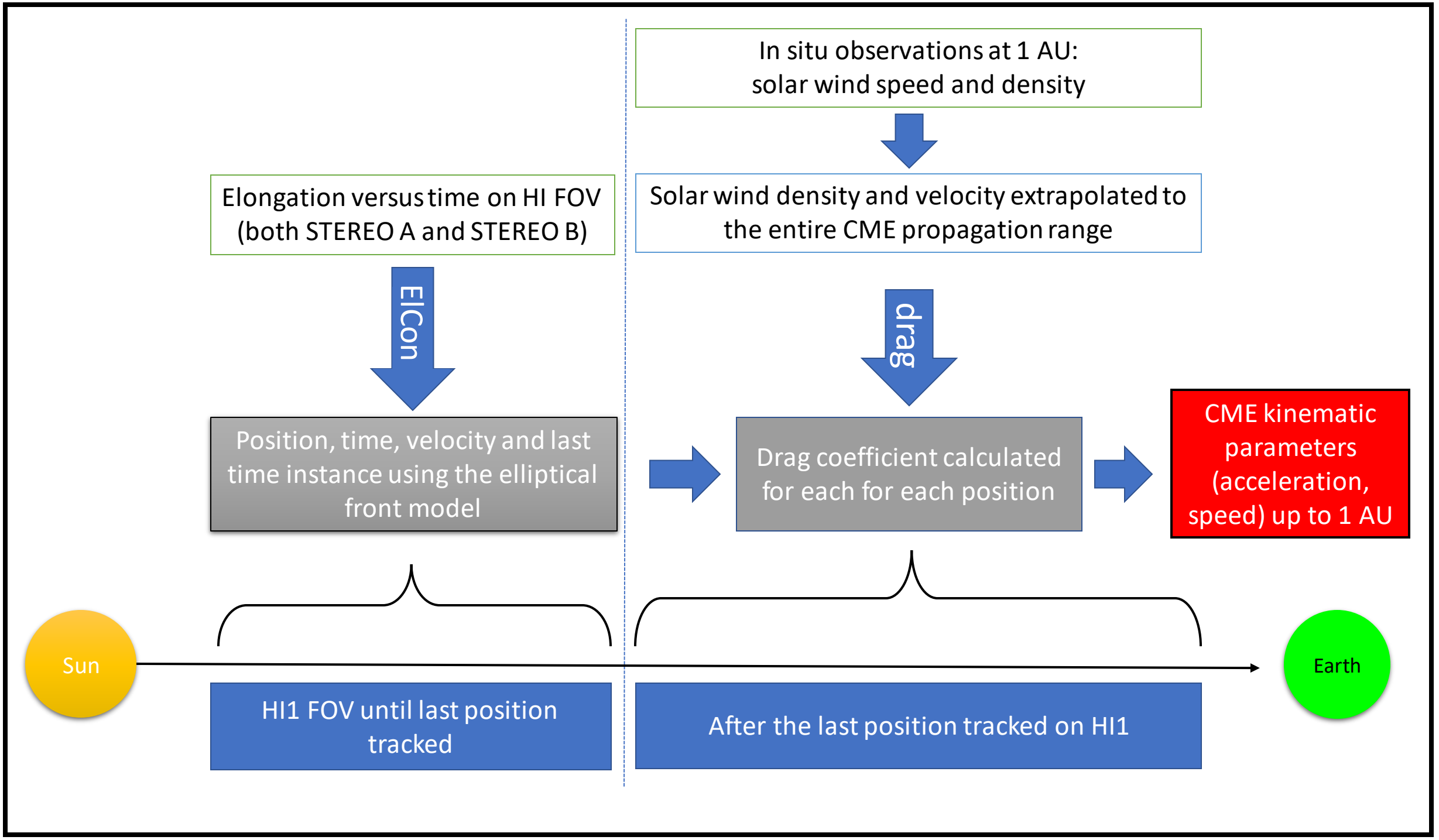
In situ observations at 1 AU:
solar wind speed and density
Elongation versus time on HI FOV
(both STEREO A and STEREO B)
Solar wind density and velocity extrapolated to
the entire CME propagation range
ElCon
drag
Position, time, velocity and last
time instance using the elliptical
front model
Drag coefficient calculated
for each for each position
CME kinematic
parameters
(acceleration,
speed) up to 1 AU
Sun
Earth
HI1 FOV until last position
tracked
After the last position tracked on HI1

Figure 4.

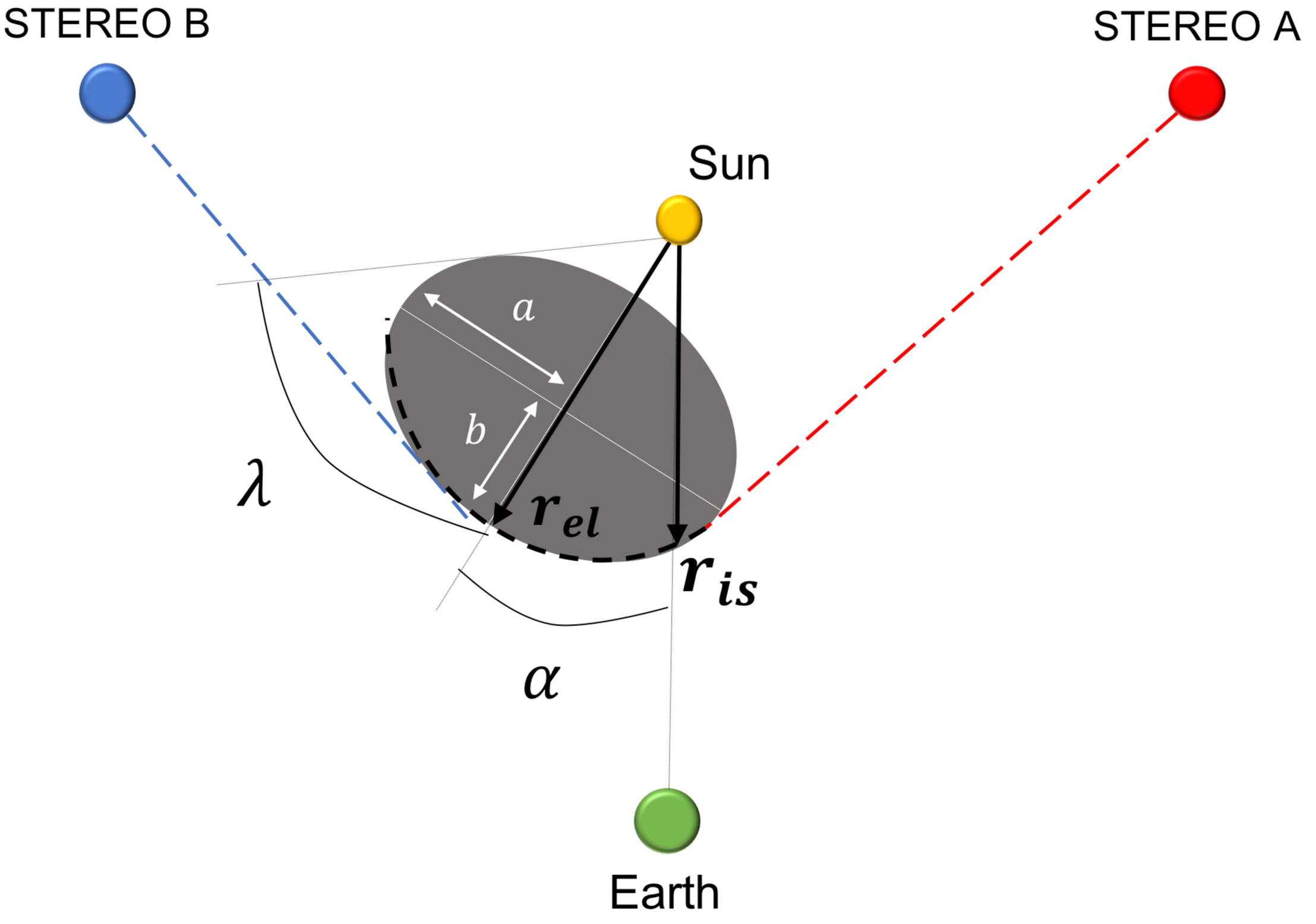
STEREO B
STEREO A
Sun
a
b
λ
r_{el}
r_{is}
α
Earth

Figure 5.

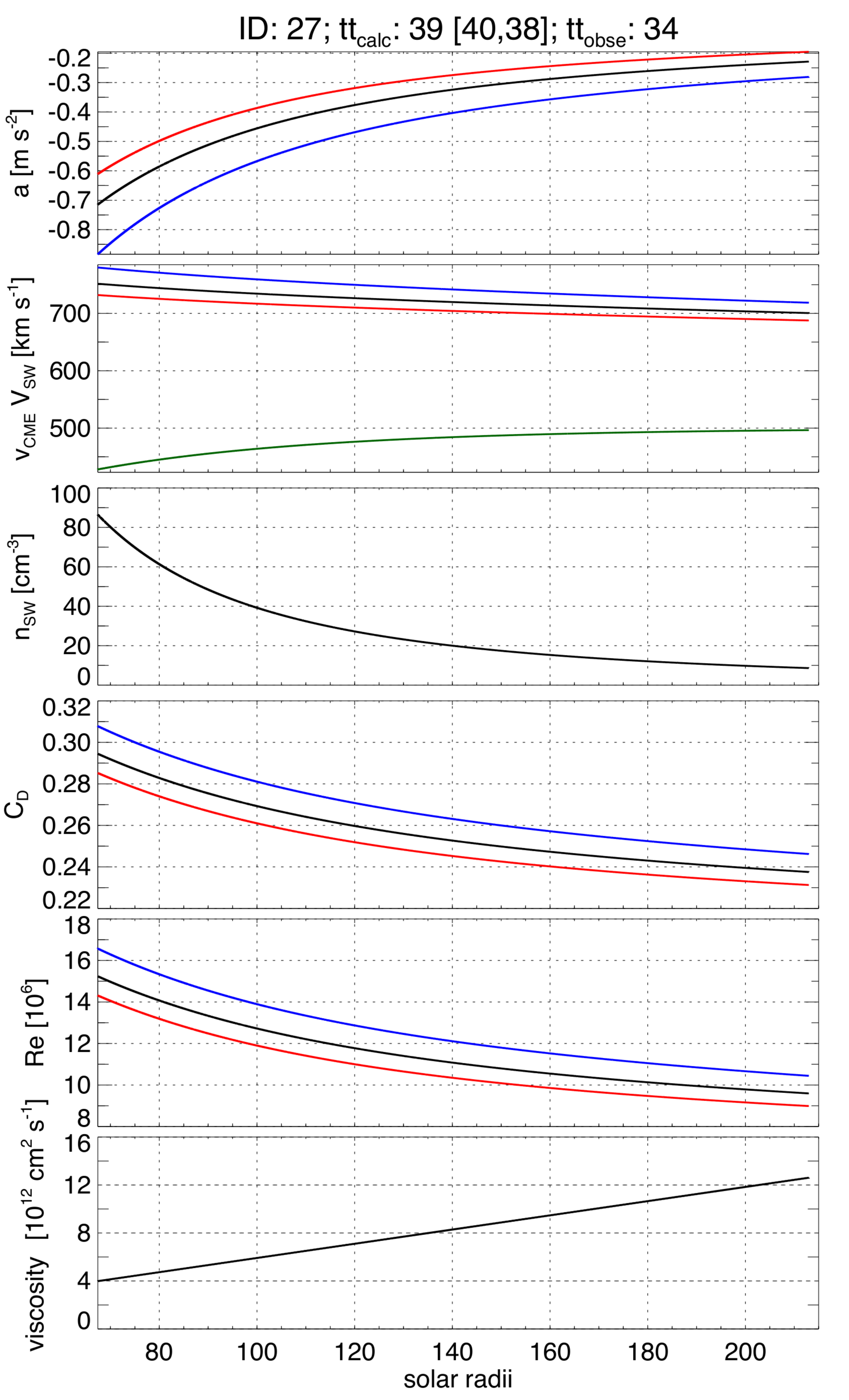
ID: 27; tt$_{calc}$: 39 [40,38]; tt$_{obse}$: 34
a [m s^{-2}]
-0.2
-0.3
-0.4
-0.5
-0.6
-0.7
-0.8
v$_{CME}$ V$_{SW}$ [km s^{-1}]
700
600
500
n$_{SW}$ [cm^{-3}]
100
80
60
40
20
0
C$_D$
0.32
0.30
0.28
0.26
0.24
0.22
Re [10^6]
18
16
14
12
10
8
viscosity [10^{12} cm^2 s^{-1}]
16
12
8
4
0
80
100
120
140
160
180
200
solar radii

Figure 6.

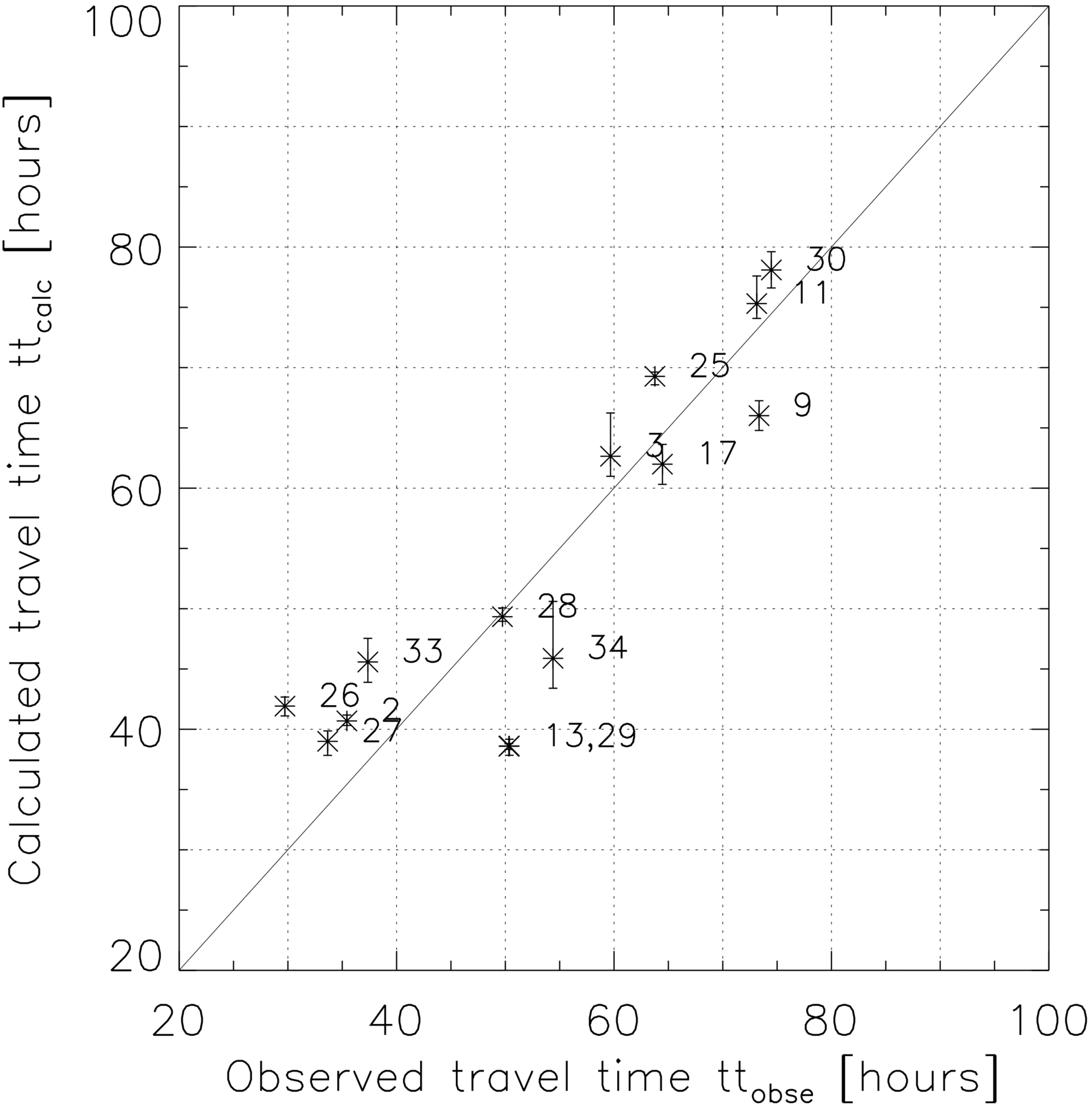
Calculated travel time tt_{calc} [hours]
Observed travel time tt_{obse} [hours]
20
40
60
80
100
30
11
25
9
3
5
17
28
34
33
26
2
27
13,29

Figure 7.

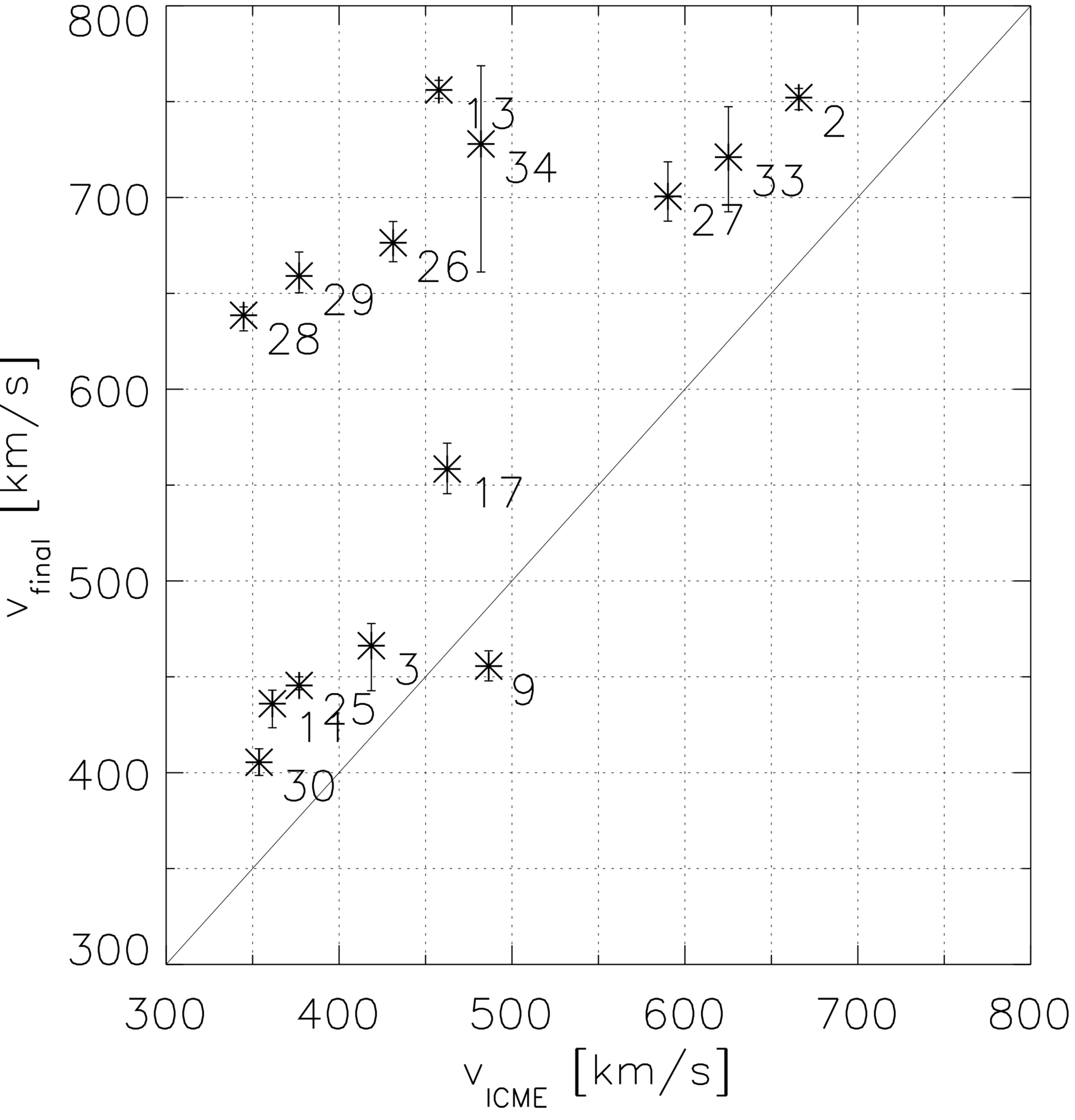
800
700
600
500
400
300
300
400
500
600
700
800
v_{final} [km/s]
v_{ICME} [km/s]
13
34
2
33
27
26
29
28
17
3
9
25
14
30